Seismological evidence of a wide low velocity zone and lower-crustal flow in the southeastern margin of Tibet based on polarity of receiver functions

Jiafu Hu, Haiyan Yang, Guangquan Li, Hengchu Peng, José Badal

PII: S1342-937X(16)30335-5
DOI: doi:10.1016/j.gr.2017.11.007
Reference: GR 1882

To appear in: *Gondwana Research*

Received date: 2 November 2016
Revised date: 10 November 2017
Accepted date: 27 November 2017

Please cite this article as: Hu, Jiafu, Yang, Haiyan, Li, Guangquan, Peng, Hengchu, Badal, José, Seismological evidence of a wide low velocity zone and lower-crustal flow in the southeastern margin of Tibet based on polarity of receiver functions, *Gondwana Research* (2017), doi:10.1016/j.gr.2017.11.007

Seismological evidence of a wide low velocity zone and lower-crustal flow in the southeastern margin of Tibet based on polarity of receiver functions

Jiafu Hu[1]*, Haiyan Yang[1], Guangquan Li[1], Hengchu Peng[1], José Badal[2]

[1]Department of Geophysics, Yunnan University, 2 North Green Lake Rd., Kunming, Yunnan, 650091 P.R. China, jfhu@ynu.edu.cn

[2]Physics of the Earth, Sciences B, University of Zaragoza, Pedro Cerbuna 12, 50009 Zaragoza, Spain, badal@unizar.es

*Corresponding author: Jiafu Hu, email: jfhu@ynu.edu.cn

Abstract

The lower-crustal flow model has become an interesting proposal to describe the growth and expansion of eastern Tibet. To date, however, the geophysical results still remain poor or partly reliable due to the non-uniqueness of the solutions found by inversion and the resolution limitations. In this study we do not invert deliberately the seismic velocity structure of the crust and upper mantle from receiver functions. Instead, we analyze the polarity of converted P-to-S phases at the Moho and the PpPs and PsPs+PpSs reverberation phases in order to get evidence of local low-velocity and lower-crustal flow in southeastern Tibet. We have obtained P receiver functions (PRFs) and S receiver functions (SRFs) using 108 permanent seismic stations deployed in the Sichuan and Yunnan areas, and we have determined the crustal thickness and Poisson's ratio. The crustal thickness provided by PRFs is consistent with the thickness given by SRFs. It varies from ~60 km in the Songpan-Ganzi

(SG) fold system and the northern part of the Sichuan-Yunnan diamond-shaped block (SYDSB), near the Eastern Himalayan Syntaxis, to ~33 km in southern Yunnan. The Poisson's ratio varies mostly from 0.24 to 0.30, although the highest values 0.28-0.30 are found along the axis formed by the Longmenshan fault, the Lijiang-Jinhe fault and the Jiali-Nujiang fault. The high value of ~0.28 in SYDSB and nearby zones is attributed to the presence of a low-velocity zone in the lower crust and hot mantle uplift, while in Sichuan Basin is attributed to the great sediment thickness. By analyzing the Ps-phase negative polarity, we have detected local low-velocity in a wide region including the east and southeast of Tibet and southern Yunnan, thus suggesting the existence of an intra-crustal low-velocity zone of complex geometry in this region. The PpPs and PsPs+PpSs reverberation phases in SYDSB and the SG fold system are clearly weaker than in the Indochina block and eastern Yunnan, thus implying that SYDSB has a different tectonic history from the Indochina block on its west side and eastern Yunnan on its east side. The above results taken together provide seismological evidence of a lower crustal flow spreading from the eastern Tibet, which in its advance southward has invaded widely SYDSB, crossed the Lijiang-Jinhe fault and reached southern Yunnan.

Keywords: receiver functions; converted crustal phases; multiple reverberations; Moho depth; Poisson's ratio; intra-crustal low-velocity zone; lower crustal flow; southeastern Tibet.

1. Introduction

The convergence and collision between the Indian and Eurasian plates over the past

50-65 million years (Molnar et al., 1993; Yin and Harrison, 2000; Tapponier et al., 2001) is undoubtedly the most spectacular and youngest case of continental collision on Earth that has given rise to the Tibet Plateau: a huge mass of nearly 2×10^7 km^2 with an average elevation of 4500 m and a crustal thickness twice the normal of around 70 km or even more (Chen et al., 2010). During this process the Tibetan Plateau has undergone a lifting of somewhat less than 4 km (Molnar and Tapponnier, 1975; Armijo et al., 1986; England and Molnar, 1997; Yin, 2000). Field observations and satellite geodesy indicate that the lifting of the Tibet Plateau has been accompanied of a small crustal shortening from the center to the southeastern margin since about 4 million years ago (Royden et al., 1997, 2008).

Global Positioning System (GPS) observations (Zhang et al, 2004; Gan et al., 2007) suggest that the upper crust movement, which collides with the barrier of the cold and rigid Sichuan Basin, is divided into two branches: one northeastward along the western boundary of the basin, and another southeastward toward Yunnan, undergoing a clockwise rotation around the Eastern Himalayan Syntaxis (EHS). These two ways account for the collision between the escape flow of eastern Tibet and the Sichuan Basin (Zhang et al., 2010), and a weak lower crust that flows over distances of 1000-2000 km from the central plateau, which makes possible the deformation of the upper crust decoupled from the movement of the underlying mantle (Royden et al., 1997; 2008).

Several models have been proposed to explain the mechanism of the surface deformation in eastern Tibet: (1) lateral extrusion of rigid blocks, in which deformation is primarily localized along strike-slip faults (Molnar and Tapponnier, 1975; Tapponnier et al., 1982); (2) continuous deformation, in which deformation distributes through a continuously

deforming lithosphere (England and Houseman, 1988); (3) lower-crustal flow, in which the strength of the lower crust is several orders of magnitude less than that of the upper crust and the mass has been flowing through the lower crust from central Tibet to Yunnan (Royden et al., 1997, 2008; Clark and Royden, 2000; Klemperer, 2006). The lower-crustal flow model seems to be feasible and is generally accepted by many geoscientists because it provides a satisfactory explanation for the topography variations and the lack of substantial shortening of the young upper crust in the eastern margin of the Tibet Plateau. Nonetheless, this model, despite its potentiality for a reasonable explanation of the regional geodynamics, is still the subject of lively debate due to the lack of reliable evidence. For example, Meltzer et al. (2007) suggested that the deformation of the lithosphere around the EHS is mechanically coupled across the crust-mantle boundary and that the lower crust is sufficiently strong to transmit stress.

Low-velocity zones in the lower crust beneath the southeastern margin of the Tibet Plateau have been detected by deep seismic soundings (Zhang et al., 2005a, 2005b; Wang et al., 2007a), body wave tomography (Wang et al., 2003; Li et al., 2008) and surface wave tomography (Yao et al., 2008, 2010). However, these proofs are not consistent enough because the reported low-velocity is relative to the global average (Yao et al., 2010). On the other hand, studies based on receiver function inversion have revealed that a shear-wave low-velocity layer, of about 10-15 km thick, extends widely in the middle-lower crust beneath most of the seismic stations installed in the southeast margin of Tibet (Hu et al., 2005; Xu et al., 2007; Wang et al., 2010; Zhang et al., 2009; 2010; 2011, 2013; Liu et al., 2014), thus supporting the validity of the lower-crustal flow model. Nevertheless, resistivity

images obtained by magnetotelluric measurements (Bai et al., 2010; Rippe and Unsworth, 2010) have emphasized that the lower-crustal flow occurs only along the Xianshuihe-Xiaojiang fault and the Jiali-Nujiang fault to the east and southeast of Tibet, respectively (Fig. 1).

According to the mismatch between GPS velocity vectors and the fast wave polarization directions of crustal anisotropy obtained by converted Ps-wave splitting analysis, Chen et al. (2013) have suggested that the eastern margin of Tibet extrudes southeastward as a whole, although the lower-crustal flow has arrived only to the Lijiang-Jinhe fault (Fig. 1). More recently, Liu et al. (2014) have used seismic data recorded by a temporary array of some 300 stations deployed in western Sichuan to investigate the eastward expansion of the Tibetan Plateau; they interpreted the crustal weak zones as crustal flow channels going beyond the Xianshuihe fault in Sichuan and the Lijiang-Jinhe fault in Yunnan (Fig. 1).

The lower crustal flow model relies on an extensive intra-crustal low-velocity zone (IC-LVZ). But a direct and firm evidence as to verify this assumption is missing due to the non-uniqueness of the data inversion process, as noted by Ammon et al. (1990). At present, the debate is focuses on two issues: (1) whether such IC-LVZ has a wide presence to the east and southeast of Tibet, and (2) whether has crossed the Lijiang-Jinhe fault and reached southern Yunnan. In this study, we have obtained P and S receiver functions from seismic data recorded at 108 permanent broadband stations deployed since 2000, which we have used to determine the crustal thickness and Poisson's ratio. We deliberately do not make use of the receiver functions to invert the velocity structure of the crust and upper mantle because of the non-uniqueness of the inversion method. Instead, we have proceeded to

analyze the polarity of converted P-to-S phases at the Moho and the PpPs and PsPs+PpSs reverberation phases on the stacked traces. Our target is to find clear seismological evidence of southeastward extrusion of east Tibet and crustal flow and its fluency mode.

2. The scenario: geodynamic framework and fault system

The agents that tectonically control the eastern and southeastern margins of Tibet are the northward subduction of the Indian plate and its movement eastward along the Burma arc and the resistance of the Sichuan Basin against the eastward extrusion of the Tibetan Plateau. Tapponnier et al. (1982, 1986) suggested that the northward motion of the India plate with respect to the Eurasia plate provoked the extrusion of large continental fragments southeastward of South China. The faults bounding these large fragments extend from eastern Tibet to southeast of Asia and connect with the opening of the South China Sea (Briais et al., 1993). During the last 4 m.y., the displacement of the crust in the southeast region of Tibet, west of the Xianshuihe-Xiaojiang fault system, has undergone a clockwise rotation around EHS due to the trench rollback of the Indian plate (Wang et al. 1998). The east-west structures in Tibet have rotated southeastward, even in north-south direction, as consequence of the extrusion of large continental fragments from central Tibet. In contrast to the southern margin of the Himalayas that is characterized by steep topographic gradients, the southeastern margin of Tibet exhibits a gradual change in topographic elevation. In the eastern margin, however, the topographic relief becomes an abrupt wall of 4 km across the Longmenshan fault.

From about 9 to 13 million years ago, lower crustal material began to flow toward the southeast margin of Tibet, inflating the crustal thickness and causing passive surface uplift (Clark and Royden, 2000; Clark et al., 2005). This material continued moving to the southeast during the Pliocene and the weak underlying lower crust reached the Xianshuihe-Xiaojiang fault system. This process, which has contributed to the continuous deformation of the lithosphere (England and Houseman, 1988), assumes the presence of weak lower crust that flows in response to lateral pressure gradients and is driven from beneath Tibet to the adjacent regions (Clark and Royden, 2000). When the flow is blocked by strong lithosphere, as happens in Sichuan basin, then a steep topographic margin arises.

A series of Cenozoic strike-slip faults, such as the Longmenshan fault, Xianshuihe fault, Lijiang-Jinhe fault, Xiaojiang fault, Jinshajiang-Red River fault, Lancangjiand fault, Jiali-Nujiang fault and Sagaing fault (Fig. 1), divide the eastern margin of Tibet into several tectonic blocks, which accommodate the collision strain. Sichuan and Yunnan are two areas located in the east and southeast margins of Tibet, respectively, where tectonics is indeed very active, as evidenced by strong seismicity and large strike-slip faults.

The Longmenshan fault (F1 in Fig. 1) in northeast direction is the boundary separating the Songpan-Ganzi fold system from the Sichuan Basin in the Yangtze Craton (Burchfiel et al., l995). Just at the edge of this fault took place the catastrophic Ms 8.0 Wenchuan earthquake on May 12, 2008 that provoked a high number of casualties and damages. The fault extends southward from the north of Longmenshan and crosses the Xianshuihe fault (F2) up to connect with the Lijiang-Jinhe Fault (F3). The Longmenshan fault is dominated by dextral strike-slip motion in the course of a long geological evolution (Burchfiel et al.,

1995, 2008). However, the average slip rate over the past 10000 years is quite low: 0.3-0.6 mm/yr of reverse motion and ~1.0 mm/yr of right-lateral strike-slip (Zhang, 2013).

The Xianshuihe fault is one of the most important strike-slip faults in the southeast of Tibet whose orientation is N40-50°W (Zhang, 2013). It extends from the SG fold belt and connects with the Xiaojiang fault (F4) to the south. The long-term slip rate of this fault is 7.5 to 11.1 mm/yr on average (Zhang, 2013). Four strong earthquakes with magnitude Ms ≥ 7.0 have occurred on the fault in the last 300 years (Allen et al., 1991), and the most recent event was the 1979 Ms 7.6 Luhuo earthquake that gave rise to a rupture surface ~90 km long.

The Jinshajiang-Red River fault (F5) is a primary fault in east Tibet that consists of several segments with northwest tendency. It starts on the east side of EHS and extends southeastward to Vietnam. The left-lateral Xianshuihe-Xiaojiang fault and the right-lateral Jinshajiang-Red River fault bound the Sichuan-Yunnan diamond-shaped block (hereafter named by its acronym SYDSB), which is regarded as the main escape block from central Tibet (Wang and Burchfiel, 2000; Tapponnier et al., 1982, 1986). Several geological studies (Wang and Burchfiel, 2000; Copley and McKenzie, 2007; Copley, 2008) make clear that the Jinshajiang-Red River fault and the Xianshuihe-Xiaojiang fault are the major tectonic boundaries that play a key role in the geodynamics of southeastern Tibet. GPS observations (Zhang et al., 2004; Gan et al., 2007) have confirmed that SYDSB moves more rapidly toward the southeast than the adjacent crust. Furthermore, SYDSB is one of the most seismically active areas in China: 169 earthquakes with magnitude 6.0≤Ms<6.9, 49 earthquakes with 7.0≤Ms<7.9 and 2 earthquakes with Ms ≥ 8.0 occurred in the block during

the period 500 to 2014 (Hu et al., 2015). Geographically, the Lijiang-Jinhe fault is the longest transverse fault that divides the block into two parts: one to the north and another further south (also diamond-shaped) (Fig. 1). This fault shows a tendency in northeast direction and a slip rate of about 3 mm/yr (Zhang, 2013).

In southeast Tibet, the Indochina block is bounded by the Jinshajiang-Red River fault and the Lancangjiang fault (F6) on the northeast side, and the Sagaing fault (F8) on the west side. The block began to extrude southeastward already in the early stages of the collision between the Indian and Eurasian plates (Tapponnier et al., 1982, 2001). The Indochina block has a high risk of earthquakes, besides volcanos and hot springs. The famous Tengchong volcano (Fig. 1) caused by the eastward subduction of the Indian plate (Lei et al., 2009), started to erupt since the Late Pleistocene, and the most recent eruption occurred about 0.01Ma ago (Wang et al., 2007b).

3. Data and method

3.1 Data selection

We collected abundant data generated by 180 teleseismic events with Ms $\geq$ 6.2 and epicentral distances between 30º and 95º (Fig. 2) for further computation of P receiver functions (PRFs). A sufficient number of earthquakes provided a large amount of seismic data, which were recorded by 108 permanent broadband stations deployed in the Sichuan and Yunnan areas to the southeast of Tibet, since 2000. To ensure receiver functions with high sign-to-noise ratio (SNR), we selected original seismic signals with a clear direct

P-wave, and discarded the waveforms with SNR< 10.0 taking the initial peak as reference. Waveforms were cut to 100 s before the phase of interest up to 20 s after.

In the same way, we followed a similar procedure for selecting seismograms for further computation of S receiver functions (SRFs). We collected S, SKS and ScS phases generated by 60 teleseismic events with Ms ≥ 6.2 and epicentral distances between 60º-85º and 85º-150º (Fig. 2), making use of traveltime tables (Kennett and Engdahl, 1991) and applying the same SNR criterion. Once made this, we cut the waveforms from 100 s before the reference phase up to 20 s after. Then the time axis was reversed such that the Sp conversion has a positive arrival time.

3.2 Data processing and receiver functions

Theoretically, effects due to the seismic source and path followed by the transmitted waves can be effectively removed from the seismogram by deconvolution, thus resulting a receiver function that mainly containing information about the crust and upper mantle beneath the recording station (Vinnik, 1977; Langston, 1977, 1979). We isolated the converted Ps phase by applying the receiver function technique (Vinnik, 1977; Langston, 1977, 1979) with 100 iterations, which originally was developed for deconvolution in time domain (Ligorría and Ammon, 1999). The set of operations aimed at getting PRFs and SRFs is similar in both cases: We practiced the rotation of the ZNE displacement components (Fig. 3). First, the north (N) and east (E) components are transformed into the radial (R) and transversal (T) components in the horizontal plane, where R is aligned with the P-wave direction and pointing to the event epicenter and T is perpendicular to R (Fig. 3a, inset in the lower right corner). Second, the radial (R) and vertical (Z) components, which lie in a same

vertical plane aligned with the incident P wave, are transformed into the L and Q components, such that the longitudinal Pp wave is polarized on the L component and the transversal Ps wave is mainly polarized on the Q component (Fig. 3a). L and Q are orthogonal in the rotated LQ system. Third, the L component is deconvolved from the Q component in time domain to thus obtain PRF and isolate the converted Ps phase.

Since the bandwidth of the sensors is in the range 0.15-25.0 Hz, we used a low-pass Gaussian filter with a width of 1.0 Hz to remove the high-frequency noise in the frequency domain after deconvolution. Then we removed all tilted waveforms and receiver functions with unclear Ps or Sp phases by visual inspection. Finally, by following the steps described up to here, we achieved 13080 PRFs from the 180 events mentioned above.

Similarly, we deconvolved the Q component from the L component by the receiver function technique (Farra and Vinnik, 2000; Yuan et al., 2006) to thus obtain SRF and isolate the converted Sp phase. SRFs have the advantage that the converted Sp wave travels faster than the incoming S wave and therefore are contamination-free by the energy associated to multiples waves. In this way, after low-pass filtering and removing indistinguishable phases, we obtained 2800 SRFs from S and SKS phases generated by the 60 teleseismic events mentioned above, with epicentral distances between 60º-85º and 85º-150º.

Fig. 3b shows a schematic view of converted P-to-S phases at the Moho and Fig. 3c shows a theoretical receiver function waveform in which Ps, PpPs and PsPs+ PpSs represent converted waves at the Moho. The time delay between these seismic phases depends on the incidence angle of the incoming wave, the velocities characterizing the medium, the number of reverberations and the depth of the discontinuity. In theory, once is known the incidence

angle, the velocity field and the number of reverberations, the time delay measurement can be used to determine the depth of the discontinuity.

3.3 Moveout correction and depth estimation

For a given discontinuity, the arrival time of a converted wave is a function of the incidence angle that is controlled by the slowness. This forces to remove the dependence of the arrival time on the epicentral distance or slowness, which is known as *moveout* correction (Dueker et al., 1997, 1998).

The time delay of the converted Ps phase from a discontinuity at depth *d*, is given by (Dueker et al., 1997, 1998)

$$T_{Pds} = \int_{-d}^{0} (\sqrt{V_s^{-2} - p^2} - \sqrt{V_p^{-2} - p^2})dz, \qquad (1)$$

where *Vp* and *Vs* denote the velocities of the P and S waves, respectively, *z* is depth, and *p* is the ray parameter. The depth of the discontinuity corresponds with the time delay associated to an incoming ray that arrives under a particular incident angle. So, before stacking waveforms, it is necessary to moveout all energy arrivals to a reference epicentral distance, e.g. a reference distance of 67º corresponding to the ray parameter or slowness p = 6.4 s/deg. For an incident ray with slowness *p*, the traveltime moveout correction for the Ps phase is

$$\Delta T_{Pds} = \int_{-d}^{0} (\sqrt{V_s^{-2} - p^2} - \sqrt{V_p^{-2} - p^2})dz - T_{Pds}^{0} \qquad (2)$$

being

$$T_{Pds}^{0} = \int_{-d}^{0} (\sqrt{V_s^{-2} - p_0^2} - \sqrt{V_p^{-2} - p_0^2})dz, \qquad (3)$$

In this expression T_{Pds}^{0} is the time delay of the converted Ps phase from a discontinuity at depth *d*, coming from a reference epicentral distance of 67º. All waveforms were moveout to the epicentral distance of reference of 67º before undertaking the stacking process. This correction makes all Ps waves almost parallel to the incident direct P-wave.

Given an earth velocity model, eq. (1) quantifies the time delay as a function of *d* and *p*. However, we still need to transform traveltime into depth. For a given value of the ray parameter, we make a table that is essentially a mapping of the Ps time delay versus the conversion depth. Thus, the amplitude of the Ps phase generated by a discontinuity at depth *d* is

$$A_i(d) = A_i(T_{Pds}^{(i)}), \qquad (4)$$

where $A_i(d)$ and $A_i(T_{Pds}^{(i)})$ are the amplitudes in the depth and time domains for the i *th* receiver function, respectively, and $T_{Pds}^{(i)}$ is the time delay for the i *th* receiver function for a discontinuity at depth *d*. This mapping helps to convert a receiver function in time domain into depth domain. The above procedure for SRFs is quite similar. Furthermore, the dominant period of the SRFs is longer than 5 s, corresponding to a wavelength of ~20 km, so that theoretically the spatial resolution may optimally reach ~6 km vertically and ~60 km horizontally (Fresnel zone at a depth of 70 km) (Li et al., 2007).

Previous results primarily obtained from seismic profiles (Zhang et al., 2009, 2010) and teleseismic receiver functions (Yang et al., 2011) indicate that the variation in crustal thickness is very sharp across the Longmenshan fault. It is indeed difficult to establish regionalized earth models for each area based on these previous results due to the absence either of P- or S-wave velocity information. For this reason, since the crustal thickness

varies largely in the study region, we considered up to three 1-D velocity models modified from the IASP91 model (Kennett and Engdahl, 1991) to convert time series into depth domain. So, to carry out all the above operations we used a first reference model for the Songpan-Ganzi fold belt and the northern part of the Sichuan-Yunnan diamond-shaped block (Fig. 1), hereafter called model A, in which the crustal thickness is 60 km. The second is for Sichuan Basin, called model B, in which the crustal thickness is 45 km. The third is for southern Yunnan, called model C, in which the crustal thickness is 35 km. In each of these models, the seismic velocity may vary slightly from the IASP91 model here adopted, without this small discrepancy can potentially affect the estimation of the thickness of the crust.

3.4 Stacking

To enhance the information contributed by weak converted phases and so increase the signal-noise ratio, an effective method consists of stacking a large amount of waveforms. Zhu and Kanamori (2000) proposed the *H-k* algorithm to determine the thickness and Poisson's ratio in the crust, in which the amplitudes of the receiver functions at the predicted traveltimes of the Ps, PpPs, and PsPs+PpSs phases, for given values of depth *H* and ratio *Vp/Vs*, are summed according to the expression

$$S(H,k) = w_1 s(t_{Ps} - t_P) + w_2 s(t_{PpPs} - t_P) - w_3 s(t_{PsPs+PpSs} - t_P) \qquad (5)$$

where $s(t)$ is the amplitude of a receiver function at the predicted time t, and $w_1 = 0.7$, $w_2 = 0.2$ and $w_3 = 0.1$ are weighing factors. The algorithm depends on the incidence mode of the wave and the depth at which the velocity discontinuity lies.

The distance to the receiver sampled by a receiver function depends on how far the signal comes and how deep the velocity discontinuity is (see Fig. 3). The multiple PpPs phases sample the structure over a distance slightly greater than the depth of the interface of interest (Ammon et al., 1990). If the Moho is the depth of interest, it means that the lateral resolution or distance swept by PRFs is roughly the crustal depth. Moreover, PRFs have the capacity to resolve even layers from 2 to 5 km thick, while the multiple reverberations allow exploring about 1 to 1.5 times the depth of the reflective interface, depending on the incidence angle to the interface (Cassidy, 1992).

4. Results

4.1 Examples of PRFs and SRFs

Here we present the results at a particular measurement point such as the TEC broadband seismic station near Tengchong (Fig. 1), where the crustal thickness is ~40 km and seems to exist a significant IC-LVZ in the crust (Yang et al., 2013). This station was installed in late 1998 as one more of the Yunnan Seismic Network, and is geographically close to the border between China and Myanmar, a zone rich in hot springs and volcanoes. After processing all seismic records generated by teleseismic events with epicentral distances ranging from 30º to 95º, we obtained 128 PRFs at the measurement point (Fig. 4a, lower panel). Before stacking, to avoid the effects derived from the different incidence of the waves, all individual seismic traces were moveout to a reference distance of 67º using the model C. Then the traces were stacked properly to increase the signal-noise ratio (Fig. 4a, top panel). The converted Pms phase at the Moho, identified at the arrival time 5.5 s, is

clearly visible whether in the stacked trace or in the individual traces. Also, multiple reverberated phases such as PpPms and PsPms+PpSms are visible. Observing Fig. 4a carefully, we can appreciate two converted phases at intra-crustal interfaces with distinct polarity, one negative at 2.0 s and the other positive at 3.6 s. Previous studies have demonstrated that the depth of the lithosphere-asthenosphere boundary (LAB) is only about 80 km, besides the existence of two to three magmatic chambers in the interior of the crust (Hu et al., 2012; Yang et al., 2013). The aforementioned negative polarity at 2.0 s implies a velocity decrease with depth, which is consistent with this tectonic setting (Lei et al., 2009; Yang et al., 2013). We applied the *H-k* algorithm (Zhu and Kanamori , 2000) to the individual receiver functions to determine the thickness and the velocity ratio in the crust. An average P-wave velocity value of 6.2 km/s for the crust (Wang et al., 2003) was applied to all stacking calculations. Fig. 4b shows the contour diagram of *Vp*/*Vs* ratio versus conversion depth at intervals of 0.5; the maximum amplitude value 8.2 at the point (39.0, 1.95) marked by a cross indicates that the crustal thickness is 39.0±1.5 km and the Poisson's ratio 1.95±0.02 at the test place.

As another application example of the *H-k* stacking algorithm, we present the results concerning MDS station, which is located at the western margin of the Sichuan Basin on the east side of the Longmenshan fault (Fig. 1). We obtained 99 PRFs at this new measurement point. These results can be seen in Fig. 4c (lower and top panel) in which the traces were stacked to increase the signal-noise ratio. The Pms phase and the PpPms phase, occurring at 6.0 s and 18.14 s, respectively, are clearly visible whether in the individual receiver functions or in the stacked waveform. However, the PsPms+PpSms phase from the Moho is

invisible either on the single receiver functions or the stacked waveform. After applying the *H-k* algorithm, the largest amplitude value 0.20 is found at the point (39.0, 1.962), but a second maximum with amplitude 0.198 occurs at the point (60.0, 1.601) in the *H-k* space (Fig. 4d). The cause of arising two optimum points with so close amplitude values is attributable to the weak amplitude of the PsPms+PpSms phase. In cases like this it is not easy to choose the optimum solution supplied by the *H-k* algorithm. To greater uncertainty, Xu et al. (2007) described two velocity discontinuities beneath MC03 station (near to MDS station), one at 44 km depth and another at 64 km, and concluded that the Moho depth should be 64 km at this location. In order to discriminate the solution provided by the *H-k* stacking algorithm in the case of weak multiple seismic phases when two extreme points are very close each other, we picked the delay time of converted phases such as Pms and PpPms to estimate an approximate value of the crustal thickness. In this way, based on the delay times of the Ps and PpPs phases at 6.0 s and 18.14 s, respectively, we calculated a crustal thickness of 37 km (Zandt and Ammon, 1995; Yang et al., 2011). According to this value nearer to one of the extreme point with larger amplitude, we chose the solution 40.0±3.1 km for crustal thickness and 1.96±0.03 for Poisson's ratio, which is consistent with previous results (Wang et al., 2007a, 2010; Zhang et al., 2010).

To quantify the error on any stacked trace we used the bootstrap method (Efron and Tibshirani, 1991) as routine procedure. If one station recorded a number N of receiver functions, we randomly chose 1–1/e (= 63%) independent receiver functions from the original data set (Liu and Gao, 2006). Then, we duplicated about the 60% of the chosen functions, so that the total number of receiver functions of the new set is the same as that of

the original set. The new receiver functions were stacked to produce images of discontinuities. We repeated this resampling process 100 times to thus generate the same number of stacked receiver functions with which compute the standard error. The black strip along each of the traces represented in Figs. 4a and 4c (top panels) gives the ±2σ error bounds (σ is standard deviation).

Due to the absence of reverberation phases in the SRFs, the *H-k* algorithm cannot be applied to estimate the crustal depth. Fortunately, for a given reference earth model, eq. (1) can help us to convert delay time into depth. The Tau-P method (Crotwell et al., 1999) was employed to get the ray parameter according to the epicentral distance. To compare the crustal thickness obtained by PRFs with that determined by SRFs, we show the 22 SRFs recorded at TEC and MDS stations (Fig. 5, lower panels), all of them after being shifted from time domain to depth domain using the model C. Of course, to avoid the effects derived from the different incidence of the waves, all individual seismic traces were previously moveout to a reference distance of 67^{o} using the model C, and then stacked to increase the signal-noise ratio (Fig. 5, top panels). The ±2σ error bounds calculated by the bootstrap method described above come given by the black strip along each of the traces represented in Figs. 5a and 5b (top panels). One positive phase in the stacked trace (Fig. 5a), occurring at 42.0±3.5 km, is labeled as S_Mp and interpreted as the converted phase at the Moho, while another negative phase, occurring at 80.0±6.0 km, is labeled as S_Lp and is interpreted as the converted phase at the LAB. In this example, the Moho depth deduced from SRFs (42.0±3.5 km) is close to the depth determined from PRFs (39.0±1.5 km). Similarly, the crustal thickness and lithospheric thickness beneath MDS station such as they

are deduced by the SRF technique are 52.0±4.0 km and 146.0±10.0 km, respectively (Fig. 5b). The crustal thickness given by PRFs is quite consistent with the thickness obtained from SRFs beneath TEC, but it is slightly smaller that the thickness obtained from SRFs beneath MDS. The deviation may be attributed to the low resolution and poor coherency of the SRFs, although the effect arising from the reference model on the results cannot be excluded.

4.2 Moho topography and Poisson's ratio

To delineate the Moho topography and the distribution of Poisson's ratio in the crust, we made use of the *H-k* algorithm (Zhu and Kanamori, 2000) on the PRFs recorded beneath each station. In this process we considered the average value of 6.2 km/s as P-wave velocity through the crust in the study area (Wang et al., 2003), and used the prediction equation (Yang et al., 2011) as a means for choosing the correct solution when there are more than one extreme points as possible solution given by the *H-k* algorithm (Zhu and Kanamori, 2000). In the case of SRFs, the available waveforms were shifted from the time domain to the depth domain and then stacked in the depth domain to obtain the Moho depth. In the following, we adopted the bootstrap method (Efron and Tibshirani, 1991) to evaluate the error in any stacked trace as well as the errors associate to the crustal thickness and Poisson's ratio.

We present the results about crustal thickness in two contour maps (Fig. 6), in which the contour lines were drawn by spline interpolation using GMT software (Wessel and Smith, 1998). The values next to the margins may not be reliable and thus are discarded for analysis. The results obtained from PRFs (Fig. 6a) and SRFs (Fig. 6b) indicate that the crust thickness varies from ~33 km in southern Yunnan to ~66 km in east Tibet. In particular, the Moho

depth decreases rapidly across the Longmenshan fault (F1 in Fig. 1), from 54-60 km beneath eastern Tibet to 36-40 km in Sichuan Basin, which highlights this fault as the natural boundary between these two regions. Also, the Lijiang-Jinhe fault (F3 in Fig. 1) marks a gradient variation zone where the Moho depth increases from 42-54 km in northern Yunnan to 57-60 km in east Tibet. Although the crustal thickness obtained by the SRF technique (Fig. 6b) depends on the reference earth model, the true is that it is very close to the thickness estimated by the PRFs technique (Fig. 6a). This consistency confirms that the reference earth model is good enough at least at the first-order approximation. The greatest discrepancy in crustal thickness does not exceed ~5 km at the southwest margin of Sichuan Basin, where the thickness varies very rapidly. The cause may be that the SRFs sample a wider lateral structure than the PRFs and lose coherency to the detriment of the individual traces. In general, the crustal thickness obtained with SRFs is 1-4 km deeper than that provided by PRFs.

Error maps based on standard deviation allow us to assess the uncertainty in crustal thickness. The errors given by PRFs (Fig. 6c) are smaller than those obtained by SRFs (Fig. 6d). The first ones are in the range 0.5-2.0 km in the Indochina block and eastern Yunnan (on the east side of the Xiaojiang fault), but they increase from 2.0-2.5 km in southern SYDSB to 3.5 km in east Tibet, and take a mean value of 3.0 km in Sichuan Basin. The second ones are in a range of 3.0-3.5 km in the Indochina block and eastern Yunnan, but they increase from 3.0-3.5 km in southern SYDSB to 5.0-5.5 km in east Tibet, and reach a moderate value of 4.0-4.5 km in Sichuan Basin. In general, the error in crustal thickness is

systematically smaller in the Indochina block and eastern Yunnan, although larger in east Tibet, while it takes a mean value in Sichuan Basin.

Poisson's ratio ranges between 0.24 and 0.32 (Fig. 7a) with standard deviation from 0.005 to 0.025; the largest deviation of 0.020-0.025 occurs in northern SYDSB, the SG block and Sichuan Basin (Fig. 7b). These Poisson's ratio values fall within the interval for common rocks, which extends from 0.20 to 0.35, depending on the mineral composition of the sample (Zandt and Ammon, 1995). The ratio decreases with the silica content, but increases with the content of mafic rock. The strong lateral variation of Poisson's ratio is completely reasonable in the study region because of its complex tectonics manifested in large faults and basins. Along the Longmenshan fault, Xianshuihe-Xiaojian fault, Lijiang-Jinhe fault and Jiali-Nujiang fault, the Poisson's ratio takes the highest values 0.28-0.30, clearly above the global average 0.24-0.25 (Zandt and Ammon, 1995). The high value (~0.28) in SYDSB and nearby zones is attributed to the presence of a low velocity in the lower crust. We will return on this issue later.

4.3 P-to-S phases within the crust

The Moho and the intra-crustal interfaces are often characterized by strong contrasts of seismic impedance, i.e. abrupt jumps in P- and S-wave velocity, as well as in density. The identification of converted phases and their multiples such as PpPs and PsPs+PpSs on the receiver functions can provide clues on the structural features of the medium. Both amplitude and time-delay of the converted phases depend on the incident angle of the perturbation and the transmission velocity in the crust, however its polarity only reflects the sign of the velocity gradient at the interface.

In order to discuss later the polarity of the converted phases, we gathered together the stacked traces according to the tectonic units that conform the study area, namely, SG fold system, Sichuan Basin, northern SYDSB, southern SYDSB, Indochina block and eastern Yunnan (on the east side of the Xiaojiang fault). In Fig. 8 we show the normalized receiver functions at different locations where we can observe the arrivals of the Ps, PpPs, and PsPs+PpSs phases, although not always the polarities of these two last phases are clear enough. The delay time among all these seismic phases satisfies the prediction equation (Yang et al., 2011). The converted phase Ps at the Moho appears clearly with positive polarity at 4-9 s behind the direct P-wave. But some of the multiple reverberations PpPs arriving later are too weak as to be identified at many stations, especially in those installed in SYDSB (Figs. 8a, 8c), the SG fold system (Fig. 8b) and Sichuan Basin (Fig. 8d). In these regions, however, there are other converted phases at intra-crustal interfaces that have positive and negative polarities. Not the case in other regions as the Indochina Block and eastern Yunnan (Figs. 8e, 8f) where the PpPs phases having positive polarity are very clear. We will return on this topic later.

5. Discussion

The receiver function technique removes the common factors of instrument response and source function from the seismogram, and is more sensitive to velocity contrasts than to the absolute magnitude of the seismic velocities (Ammon et al., 1990). It is applied to the delay time of the conversion phase at a discontinuity to determine its depth. However, the dip of the layer and anisotropy of the medium produce a response both on the arrival time

and amplitude of the conversion phase that varies with the backazimuth (Hayes and Furlong, 2007). For instance, the amplitude of the converted Ps phase is maximum when the backazimuth is aligned with the up-dip direction, and minimum if the wave arrives in down-dip direction, and the arrival times also vary in the two cases. This effect is most pronounced for structures with a dip angle greater than 30º (Cassidy 1992). Nonetheless, this hardly influences our case because we work with teleseismic events that cover a wide range of azimuthal values and whose epicentral distances are generally larger than 45º (Fig. 2), so that generate almost vertical energy arrivals. Although previous studies indicate that the Moho depth varies strongly in the southeast margin of Tibet (Hu et al., 2005; Xu et al., 2007; Zhang et al., 2009, 2010; Wang et al., 2010), the dip angle of the Moho is significantly smaller than 30º. Therefore, the effects derived from the aforementioned factors are effectively reduced and still more after summation of individual waveforms.

5.1 Crustal thickness

The elevated topography of the eastern margin of Tibet has been explained as a direct result of the crustal thickening by lower-crustal flow evacuated from beneath central Tibet (Royden et al., 1997; Clark and Royden, 2000). Despite the lack of significant shortening observed in the upper crust (Burchfiel et al., 1995; Wang and Burchfiel, 2000), the topographic elevation gradient is interpreted to be the effect of the driving force that maintains such crustal flow (Royden et al., 1997; Clark and Royden, 2000). The comparison of the crustal thickness obtained from P and S receiver functions (Fig. 6) with the topographic elevation (Fig. 1) allows us to observe the same variation tendency, although the thickness deduced from SRFs is generally 1 to 4 km (in some sites even a bit more) thicker

than that obtained from PRFs. An important structural feature is that the crustal thickness of 36-40 km under Sichuan Basin becomes 54-60 km when passing to SG fold system in eastern Tibet, confirming that the Longmenshan fault is the natural boundary separating eastern Tibet from the Yangtze Craton.

The Moho depth determined from this study is consistent with other previous results deduced from PRFs (Hu et al., 2005; Xu et al., 2007; Zhang et al., 2009, 2010; Wang et al., 2010); the difference to emphasize is that these latter come from linear profiles or temporary stations and thus are limited spatially or in amount with respect to the ours. In Yunnan region, the crustal thickness varies from ~33 km in southern Yunnan to ~60 km in the northwest (Fig. 6a); these results are consistent with those deduced from deep seismic soundings (Zhang et al., 2005a, 2005b; Zhang and Wang, 2009). The Lijiang-Jinhe fault, which divides the Sichuan-Yunnan diamond-shaped block into two parts (F3 in Fig. 1), is another geological boundary with a notable variation in the topographic relief on both sides: the topographic elevation of 3500-4000 m in the eastern margin of Tibet decreases to 2000-2500 m south of the fault. Our results also indicate an equivalent gradual variation in the thickness of the crust.

Previous gravity measurements have revealed a NE-SW Bouguer anomaly belt of some 150 km wide and 900 km long approximately, extending along the Longmenshan fault and the Lijiang-Jinhe fault in the interior of Yunnan (Wang et al., 2003). The Bouguer anomaly decreases from -200 mGal in southeastern Yunnan to -460 mGal in east Tibet. This gravity pattern fit well with our results about crustal thickness that also show a more or less similar strong gradient (Fig. 6a).

5.2 IC-LVZ

The 108 permanent broadband stations deployed in Sichuan and Yunnan region (Fig. 9) are installed on bedrock and hard soil, so that the recorded data are hardly affected by the human activity. So, the sign-to-noise ratio on seismograms is higher than with temporary stations for the same events (Xu et al., 2007), which facilitates the polarity analysis of the phases on the stacked traces (Fig. 8). The polarity of the Moho converted Ps phases provides information on the velocity contrast on both sides of this important discontinuity (Hazarika et al., 2012). Generally, a positive polarity of Ps indicates a positive velocity gradient with depth and conversely if the polarity is negative. However, the response of the P-to-S multiples (PpPs, PsPs+PpSs with negative polarity) to a dipping structure is more complicated than that of the direct converted Ps wave and greatly depends on the dip and depth of the interface, ray parameter and back azimuth. Because of these complications with real data and to minimize such uncertainties, our analysis on the polarity of P-to-S phases is confined to the first seconds of the receiver functions.

Based on the polarity of the converted phases, we have identified numerous low-velocity sites spread all over the study area (Fig. 9, red circles) together with other ones with a weak PpPs phase (Fig. 9, blue circles). These sites are found west of Sichuan Basin, but not in the basin itself, and some low-velocity points are located east of the major Xianshuihe-Xiaojiang faults and west of the Jinshajiang-Red River fault, besides in the interior of SYDSB. Xu et al., (2007), by inversion of S velocity from PRFs at 25 temporary broadband seismic stations deployed in the southeastern margin of Tibet, found six stations with local IC-LVZ (Fig. 9, red squares, with MC0 prefix), in agreement with our results.

This means that low velocities have a wide presence to the east and southeast of Tibet, and in southern Yunnan after crossing the Lijiang-Jinhe fault. Our results are also consistent with other previous results obtained from receiver function migration and inversion profiling across the Longmenshan belt (Zhang et al., 2009; Wang et al., 2010), as well as with results from joint inversion of receiver functions and surface waves (Liu et al., 2014). Surface wave inversion has revealed that shear-wave speed is relatively low in the entire crust, even anomalously low in the deep crust in comparison with the average crust beneath southeastern Tibet (Yao et al., 2010). This seems to indicate a rather heterogeneous distribution of the IC-LVZ in the region.

The presence of local low-velocity all over the study region has its correlation with the existence of a mechanically weak middle-lower crust in the southeastern margin of Tibet supported by wide-angle seismic profiling (Zhang et al., 2005a, 2005b; Wang et al., 2007a; Zhang and Wang, 2009), low electrical resistivity (Bai et al., 2010), high heat flow (Hu et al., 2000) and high Vp/Vs ratio (Xu et al., 2007), which are indicators of the existence of partial melt and viscosity reduction in the middle-lower crust and evidence of crustal flow.

Magnetotelluric profiles performed by Bai et al. (2010) in the region have revealed some high conductivity sites in the crust (Fig. 9, blue ellipses) that correlate with some of our stations where we have detected IC-LVZ; for example at TEC station near the Tengchong volcano area, in western Yunnan, where there are several low-velocity sites (Fig. 9). Nevertheless, these low-velocity points in western Yunnan should be attributed to the eastward subduction of the Indian plate (Lei et al., 2009), which certainly impinges on the mantle dynamics and suggests a large-scale IC-LVZ spreading out from eastern Tibet.

Recently, Fan et al. (2015) have found Rayleigh-wave group velocity (in the range 30-48 s) 0.2 to 0.3 km/s higher in southwestern Yunnan, i.e. on the west side of the Jinshajiang-Red River fault (F5 in Fig. 1), than on the east, in southern SYDSB. Also recently, Bao et al. (2015), using data recorded in more than 300 stations under the ChinArray program, and by joint inversion of Rayleigh-wave dispersion and receiver functions, have got a high-resolution 3D image that reveals the distribution of low velocity zones in the study area. The prominent features are two low-velocity channels A and B (Fig. 9, highlighted in yellow) bounded by major strike-slip faults around the EHS and in the southeastern margin of Tibet, the latter (channel B) extending a bit beyond the Xiaojiang fault. This is consistent with resistivity imaging by magnetotelluric measurements (Bai et al., 2010; Rippe and Unsworth, 2010), but not with other previous results (Hu et al., 2005; Xu et al., 2007; Yao et al., 2010). As can be seen, many of the stations (not all) in which we have detected IC-LVZ are included within those two channels A and B, but also numerous stations are outside, and this leads us to suggest the existence of a wide IC-LVZ that reaches the south part of the SYDSB block. It is very possible that it is a reliable clue of lower-crustal flow that even would go beyond the Xiaojiang fault (F4 in Fig. 1) according to our observations of low velocity points (Fig. 9). But if so, such crustal flow would have exceeded the Xiaojiang fault by very little, if we just look at that very few earthquakes have occurred in eastern Yunnan (Fig. 1). Not so in western Yunnan where seismicity is associated to the eastward subduction of the Indian plate and the resulting rollback westward at the LAB (Lei et al., 2009).

Since the Pms phase is generated at the Moho and the wave paths are confined within the crust only, Pms splitting can provide the most direct constraints on the anisotropy and deformation of the crust. Chen et al. (2013) have studied the seismic anisotropy by analyzing Pms-phase splitting in the explored area: a minimum part of anisotropy can be attributed to the upper crust, while the primary source of the anisotropy strength has its origin in the middle-lower crust as consequence of the stress field and deformation within these crustal layers. Sun et al. (2013) selected high-quality Pms phases from PRFs recorded at 21 temporary seismic stations deployed in southwestern Yunnan and obtained 283 splitting parameters. Their results indicate that the average fast wave polarization direction points southeastward (Fig. 10). In the northernmost Indochina block, the directions of the GPS velocity vectors (Zhang et al, 2004; Gan et al., 2007) differ largely from those of the crustal anisotropy which, makes clear that likely the upper crust and middle-lower crust are mechanically decoupled, unlike the interpretation of Bai et al. (2010) and Bao et al. (2015). These results based on Pms-phase splitting measurements come to support the existence of material flow southeastward across the deepest layers of the crust, rather than the clockwise rotation of the lower crust around the EHS (Bai et al., 2010; Bao et al., 2015). The reason is that the Pms phase splitting measurements primarily reflect the deformation mechanism of the lower crust (Chen et al., 2013).

5.3 Poisson's ratio

Two areas show a high Poisson ratio of 0.28-0.30 near Sichuan, one is roughly distributed along the Longmenshan fault and the other along the Xianshuihe fault (Fig. 7). Previous results also obtained from receiver functions give Poisson's ratio values of

0.29-0.32 along the Longmenshan fault (Zhang et al., 2009; Wang et al., 2010), clearly over the global average (Christensen and Mooney, 1995; Christensen, 1996). Xu et al. (2007) estimated a ratio of 0.29-0.32 in the west of Sichuan Basin, near the Xianshuihe fault, which are somewhat higher values than ours. Sichuan Basin is an ancient and intact part of the Yangtze Craton that remains relatively stable despite several orogenic episodes around it during the Mesozoic and Cenozoic epochs (Schoenbohm et al., 2006). The high Poisson's ratio observed in the northwest of the basin may be attributed to sediments ~10 km thick. This has its correlation in the stacked traces in Fig. 8d, where a clear converted phase is very close to the direct P-wave at stations JMG, BZH, JJS and XCO.

In Yunnan the Poisson's ratio is high, 0.28-0.30, and is distributed along the Lijiang-Jinhe fault and the Nujiang fault, and also along the north segment of the Xiaojiang fault (Fig. 7). In central Yunnan a north-south trending belt shows a Poisson's ratio of 0.24-0.26, close to the global average value (Christensen and Mooney, 1995; Christensen, 1996). The Tengchong volcano area in western Yunnan has a very high Poisson ratio of 0.30 (Fig. 7). These values keep some correlation with the heat flow (Hu et al., 2000), which also varies greatly in Yunnan. The heat flow changes from 50-80 mW/m^2 near the Sichuan area and the basin itself to 40-50 mW/m^2 in southern Yunnan; and from 100 mW/m^2 in western Yunnan, where there are volcanoes and hot springs, to 60-80 mW/m^2 in the south part of the SYDSB block (Hu et al., 2000).

The variation of the Poisson's ratio may be caused by differences in composition of the materials, temperature, or even by the faulting regime (allowing for shear motion). The relatively high values (0.28-0.30) observed along the Longmenshan-Lijiang-Jinhe faults

could be attributed to ultramafic rocks or eclogites (thrusting upwards the Tibetan lower crust). The high Poisson's ratio (0.28-0.30) in SYDSB and around may result from the presence of fluids in the lower crust (Yuan et al., 1997).

Lei et al. (2014) have made a P-wave velocity map of the uppermost mantle in the east and southeast of Tibet. Fig. 10 shows this map for a reference velocity of 8.0 km/s that to some extent resembles the Poisson's ratio pattern (Fig. 7). It can be observed a low-velocity anomaly, as low as ~7.7 km/s, running from the SG block, along the Lijiang-Jinhe fault, and reaching the southern part of SYDSB. The consistency with the spatial distribution of high Poisson's ratio suggests the presence of hot upper mantle material that would reduce the seismic wave velocity in the crust.

5.4 Polarity modeling of converted phases

In principle, the minimum velocity difference on both sides of an interface to generate an observable Ps phase depends on the receiver function noise level and the incidence angle of the incoming wave on the boundary (Ammon, 1991). Previous results already have demonstrated that the minimum detectable velocity contrast should be within the range 0.2 to 0.4 km/s (Cassidy, 1992). We have alluded earlier to the polarity of the converted phases to discern about the existence or not of an IC-LVZ. We have assumed that if the first phase arriving behind the direct P-wave has negative polarity it implies the presence of an IC-LVZ. But now we wonder to what extent a seismic phase with negative polarity reasonably indicates an IC-LVZ. With this purpose we chose some representative seismic stations that show phases with and without negative polarity to directly invert radial PRFs for shear wave velocity. We started from moveout correction waveforms to a reference distance of 67º and

then stacked in only one average trace, and used the linearized inversion technique in time domain (Ammon et al., 1990) with each of these stacked traces. In any case the parameterization of the initial model was based on known velocity data and was performed by thin, homogeneous and horizontal layers of equal thickness (2 km). Fig. 11 shows the S-wave velocity models obtained by receiver function inversion at some stations, namely: HUP and YIM in the Sichuan-Yunnan diamond-shaped block; JMG in Sichuan Basin; YOD in the Indochina block and LOP in eastern Yunnan. The dotted lines show the respective initial models for inversion. To have a measurement of the reliability of these results, we calculated the adjustments between radial and synthetic waveforms computed by forward modeling. In the lower panels can be seen the adjustments between radial and synthetic waveforms computed by forward modeling. All these fits can be seen in the lower panels in Fig. 11 and all of them are above the 90%.

First, we selected three stations located in two very different sites and far away from each other, where a negative phase has been observed after the direct P-wave in the PRFs waveforms: JMG in the Sichuan Basin (Fig. 8d); HUP and YIM in the Sichuan-Yunnan diamond-shaped block (Fig. 8c). The respective initial models for these blocks are taken from deep seismic profiles (Wang et al., 2007a) and inversion results (Liu et al., 2014). After viewing the S-wave velocity models obtained by receiver functions inversion, it can be seen a significant IC-LVZ of about 20 km thick beneath HUP and YIM (Figs. 11a, 11c). However, despite having negative polarity after the direct P-wave at JMG station, no IC-LVZ is now observed in the corresponding model (Fig. 11b). The reason is none other than Sichuan Basin is a stable and rigid craton (Burchfiel et al., l995; Schoenbohm et al., 2006).

Nonetheless, a low-velocity sediment layer of 1.5-2.5 km/s is found beneath JMG. When a sediment layer is introduced, the first significant negative polarity behind the direct P-wave does not represent any IC-LVZ because multiple reverberations between the surface and the bedrock cause this polarity. In fact, the peak of the first arrival (Fig. 8d) looks wider due to the effect of the sediment, i.e. a positive arrival at ~1 s coming from the bedrock is superposed causing a greater width of the peak of the first arrival (Hazarika et al., 2012). Similar cases can be found in the stacked traces at other stations, for example at BZH and JJS (Fig. 8d).

Second, we selected other two stations YOD and LOP, the former located in the Indochina block and the latter in eastern Yunnan; in neither of them is observed a negative phase after the direct P-wave in the corresponding waveforms. (Figs. 8e, 8f). In relation to these two regions, the initial models for S-velocity inversion are based on surface wave array tomography in SE Tibet (Yao et al., 2008, 2010) and receiver functions (Hu et al., 2005; Wang et al., 2010; Liu et al., 2014). As expected, the inversion results indicate now that there is no IC-LVZ beneath the two selected stations (Figs. 11d, 11e), which agrees with the absence of a negative polarity phase after the direct P-wave. Furthermore, the average crustal velocity beneath the Indochina block is less than in Yunnan, and the Moho is not as sharp as in eastern Yunnan, which may be due to the heating of the upper mantle in Indochina (Lei et al., 2014).

The results obtained after modeling the polarity of some phases indicate that only the first converted phase after the direct P-wave is reliable for interpretation due to the interference of multiple reverberations (Hazarika et al., 2012). Unlike the Indochina block

(on the west side of the Jinshajiang-Red River fault) and eastern Yunnan, where the PpPs reverberation phases are very clear (Figs. 8e, 8f), these phases appear masked in SYDSB (Figs. 8a, 8c) and the SG fold system (Fig. 8b) and also in Sichuan Basin (Fig. 8d), probably by negative phases coming from the top of a not very thick intra-crustal interface, and therefore are too weak as to discern whether there is or not a sediment layer or a LVZ in the crust. We pay more attention to this in the next section.

5.5 Reverberation phases and implications

Be a model consisting of a crust with P and S velocities of 6.0 km/s and 3.5 km/s, respectively, and density of 2.8 g/cm^3; and a mantle with velocities of 8.0 km/s and 4.6 km/s, and density of 3.3 g/cm^3. Supposing an incoming P wave coming from a distance of 67º, the computation of theoretical converted phases, Ps, PpPs and PsPs+PpSs, gives amplitudes equal to 0.15, 0.14 and -0.14, respectively, which obviously are very close each other. But this is not so evident in practice. Cassidy (1992) conducted a thorough analysis of the effects of tilted layers on receiver functions, and noted that these layers produce an effect on the amplitude and delay time of multiple reverberations, and that this effect is more pronounced for structures with a dip angle greater than 30º.

For northern SYDSB, southern SYDSB and the SG block, a prominent feature is that the Ps phase is clearly visible, but the PpPs phase is too weak to be identified (Figs. 8a-c). We have 19 stations with weak or invisible multiple reverberations in SYDSB and the SG block, although we have estimated an IC-LVZ in 11 of them. The PpPs phase refers to an S wave that travels once within the crust and it samples a longer radial distance than the PsPs+PpSs phase (see Fig. 3), so that its amplitude in the stacked trace may be easily

influenced by factors such as a tilted layer or partial melt within the crust. The PsPs+PpSs phase refers to an S wave that travels twice within the crust, by which it may be easily affected by partial melt around the station. The weak PpPs phase recorded at those 11 stations is probably the result of a complex structure of the crust that contains a mechanically weak layer. The remaining 8 stations with weak multiples waves, which do not reveal any IC-LVZ, are all on a crustal thickness gradient belt, and the reason of the weak multiple reverberations may be attributed to a tilted Moho (Fig. 6). However, both GZA and SMI are stations showing weak reverberations (Figs. 8b, 8d) besides an IC-LVZ, by which is difficult to ignore the hypothesis of a low velocity layer along with a tilted Moho, since the two stations are located on a crustal thickness gradient belt.

A soft shallow structure can mask P and S waves and provoke the decreasing of their amplitudes (Cassidy, 1992). The hardly visible PpPs phases related to Sichuan Basin (Fig. 8d), which is a cold rigid block of the Yangtze Craton (Copley, 2008, Li et al., 2008), should be attributed to sediment, rather than to a low-velocity zone in the crust. Interestingly, the stacked traces show clear Ps phases, except for WCH station at the edge of the basin, where the Ms 8.0 Wenchuan earthquake occurred on May 12, 2008. The Ps phase at this station presents small amplitude and a certain width (Fig. 8b), implying that the Moho is a gradual discontinuity, or partial melt within the lower crust, rather than a sharp velocity jump.

In contrast, the PpPs and PsPs+PpSs phases are very sharp in the Indochina block on the west side of the Jinshajiang-Red River fault (Fig. 8e) and in eastern Yunnan on the east side of the Xiaojiang fault (Fig. 8f). These phases are free from contamination by other phase, and reflect a structure of the crust simpler than in SYDSB. Although an IC-LVZ exists

around the Tengchong volcano area (see TEC station in Fig. 9), the lateral extension of this zone is perhaps too small to affect multiple reverberations. The typical features of the PRFs provide a clue that the Indochina block and eastern Yunnan have a crustal structure that largely differs from that of SYDSB and the SG block have. Such difference may be the result that these two large regions have undergone a different tectonic history. Xu et al. (2007) drew the attention on a negative phase between 0 and 5 s immediately after the direct P-wave that they interpreted as an IC-LVZ in SYDSB. This block would have been directly extruded from the central Tibet (Molnar and Tapponnier, 1975; Tapponnier et al., 1982) and after a flow of ductile material would have been injected into the lower crust below SYDSB, as described by Clark and Royden (2000) and Clark et al. (2005). In this regard, Liu et al. (2014) concluded that a rigid block motion and crustal flow are not irreconcilable modes of crustal deformation in southeastern Tibet.

Limiting ourselves to the distribution map of negative polarity and the many sites where we have observed low velocity, we suggest that the lower-crustal flow coming from eastern Tibet is widely spread and has reached southern Yunnan. This conclusion differs from that of Chen et al. (2013) that the lower-crustal flow has reached only the Lijiang-Jinhe fault; and also from that of Bai et al. (2010) and Bao et al. (2015) that the flow is constrained within two arc-shaped low-velocity channels along the Xianshuihe-Xiaojiang fault and the Jinshajiang-Red River fault.

6. Conclusions

We have analyzed PRFs and SRFs from 108 permanent seismographic stations deployed in Sichuan and Yunnan, with the target of getting seismological evidence of the low-velocity distribution and eventually of the lower-crustal flow in the southeastern margin of Tibet. We have obtained important results concerning the lithosphere structure and Poisson's ratio. The crustal thickness is consistent with the Bouguer gravity anomaly and the Moho topography varies from ~60 km in the Songpan-Ganzi fold system and northern SYDSB to ~33 km in southern Yunnan. The Poisson's ratio varies between 0.24 and 0.30 in the southeast Tibet-Yunnan area, but it takes the highest values (>0.28) along the large faults of Longmenshan, Xianshuihe-Xiaojian, Lijiang-Jinhe and Jiali-Nujiang, coinciding with a Pn-wave high-velocity zone. High values (~0.28) in SYDSB and nearby zones may be the result from an intra-crustal low-velocity zone and the presence of hot upper mantle. To this respect we can say that there is a good correlation between Poisson's ratio and heat flow in Yunnan; this latter varies noticeably passing from 40-50 mW/m^2 in southern Yunnan to 100 mW/m^2 in western Yunnan.

The first converted phase having negative polarity and arriving immediately behind the direct P-wave is interpreted to be a qualitative indicator of the existence of a low-velocity zone in the crust. In this way, the converted Ps phase immediately behind the direct P-wave at most of stations in the western Songpan-Ganzi block and SYDSB is interpreted that comes from an IC-LVZ beneath the stations. Our results reveal that a wide IC-LVZ underlies beneath this region, and that is not constrained within two arc-shaped low-velocity channels along the Xianshuihe-Xiaojiang fault and the Jiali-Nujiang fault, as has been noted. Nonetheless, the strong lateral heterogeneity in the region implies a complex geometry of

this IC-LVZ, which is difficult to image because of the small number of stations near latitude 29ºN. The PpPs and PsPs+PpSs reverberation phases are very clear in the Indochina block and also in eastern Yunnan, and seem to directly exclude the existence of an IC-LVZ in these two areas.

In contrast to the sharp PpPs and PsPs+PpSs phases on the west side of the Jinshajiang-Red River fault and on the east side of the Xiaojiang fault, the weak PpSs+PsPs phases in SYDSB are a clear evidence in support of a crustal flow coming from the Tibetan Plateau, which in its advance southwards has invaded widely the Sichuan-Yunnan diamond-shaped block, crossed the Lijiang-Jinhe fault and reached southern Yunnan. In this framework, the Xianshuihe-Xiaojiang fault and the Jinshajiang-Red River fault, eastern and western boundaries of SYDSB, seem to channel the movements of ductile material southeastward and southwestward, respectively, thus playing a key role in the rigid extrusion and accommodation of the lithospheric deformation during the expansion of eastern Tibet.

Acknowledgements

We thank two anonymous reviewers for their helpful comments and constructive suggestions that made possible a better presentation of this paper. We gratefully acknowledge the financial support for this work contributed by the National Natural Science Foundation of China (grants 41304076, 41374106 and 41464003).

References

Allen, C.R., Lou, Z., Qian, H., Wen, X., Zhou, H., Huang, W., 1991. Field study of a highly active fault zone: the Xianshuihe fault of southwestern China. Geol. Soc. Am. Bull. 103, 1178-1199.

Ammon, C.J., Randall, G.E., Zandt, G., 1990. On the non-uniqueness of receiver function inversions. J. Geophys. Res. 95(B10), 15303-15318.

Ammon, C. J., 1991. The isolation of receiver effects from teleseismic P waveforms, Bull. Seism. Soc. Am. 81, 2504-2510.

Armijo, R., Tapponnier, P., Mercier, J.L., Han, T.L., 1986. Quaternary extension in southern Tibet: field observations and tectonic implications. J. Geophys. Res. 91, 13803-13872.

Bai, D., Unsworth, M., Meju, M., Ma, X., Teng, J., Kong, X., Sun, Y., Sun, J., Wang, L., Jiang, C., Zhao, C., Xiao, P., Liu, M., 2010. Crustal deformation of the eastern Tibetan Plateau revealed by magnetotelluric imaging. Nat. Geosci. 3, 358-362.

Bao, X., Sun, X., Xu, M., Eaton, D.W., Song, X., Wang, L., Ding, Z., Mi, N., Li, H., Yu, D., Huang, Z., Wang, P., 2015. Two crustal low-velocity channels beneath SE Tibet revealed by joint inversion of Rayleigh wave dispersion and receiver functions. Earth Planet. Sci. Lett. 415, 16-24.

Briais, A., Patriat, P., P Tapponnier, P., 1993. Updated interpretation of magnetic anomalies and seafloor spreading stages in the South China Sea: implications for the Tertiary tectonics of Southeast Asia. J. Geophys. Res. Solid Earth 98 (B4), 6299-6328.

Burchfiel, B.C., Chen, Z., Liu, Y., Royden, L.H., 1995. Tectonics of the Longmen Shan and adjacent regions, Central China. International Geology Review 37, 661-735.

Burchfiel, B.C., Royden, L.H., van der Hilst, R.D., Hager, B.H., Chen, Z., King, R.W., Li, C., Lü, J., Yao, H., Kirby, E., 2008. A geological and geophysical context for theWenchuan earthquake of 12 May 2008, Sichuan, People's Republic of China. GSA Today 18, 4-11.

Cassidy, J. 1992. Numerical experiments in broadband receiver function analysis, Bull. Seism. Soc. Am. 82(3), 1453–1474.

Chen, Y., Badal, J., Hu, J., 2010. Love and Rayleigh wave tomography of the Qinghai-Tibet Plateau and surrounding areas. Pure Appl. Geophys. 167(10), 1171-1203.

Chen, Y., Zhang, Z., Sun, C., Badal, J., 2013. Crustal anisotropy from Moho converted Ps wave splitting analysis and geodynamic implications beneath the eastern margin of Tibet and surrounding regions. Gondwana Research 24, 946-957

Christensen, N.I., Mooney, W.D., 1995. Seismic velocity structure and composition of the continental crust: A global view. J. Geophys. Res. 100, 9761-9788.

Christensen, N.I., 1996. Poisson's ratio and crustal seismology. J. Geophys. Res. 101, 3139-3156.

Clark, M.K., Royden, L.H., 2000. Topographic ooze: Building the eastern margin of Tibet by lower crustal flow. Geology 28 (8), 703-706.

Clark, M.K., House, M.A., Royden, L.H., Whipple, K.X., Burchfiel, B.C., Zhang, X., Tang, W., 2005. Late Cenozoic uplift of southeastern Tibet. Geology 33(6), 525-528.

Copley, A., McKenzie, D., 2007. Model of crustal flow in the India-Asia collision zone. Geophys. J. Int. 169, 683-698.

Copley, A., 2008. Kinematics and dynamics of the southeastern margin of the Tibetan Plateau. Geophys. J. Int. 174, 1081-1100

Crotwell, H.P., Owens, T.J., Ritsema, J., 1999. The TauP toolkit; flexible seismic travel-time and ray-path utilities. Seismol. Res. Lett. 70(2), 154-160.

Dueker, K.G., Sheehan, A.F., 1997. Mantle discontinuity structure form midpoint stacks of converted P to S waves across the Yellowstone hotspot tract. J. Geophys. Res. 102, 8313-8327.

Dueker, K.G., Sheehan, A.F., 1998. Mantle discontinuity structure beneath the Colorado Rocky Mountains and High Plains. J. Geophys. Res. 103, 7153-7169.

Efron, B., Tibshirani, R., 1991. Statistical data analysis in the computer age. Science 253, 390-395.

England, P.C., Houseman, G.A., 1988. The mechanics of the Tibetan Plateau. Royal Society of London Philosophical Transactions, ser. A 326,301–320.

England, P., Molnar, P., 1997. Active deformation of Asia: from kinematics to dynamics. Science 278, 647-650.

Fan, L.P., Wu, J.P., Fang, L.H., Wang, W.L., 2015. The characteristics of Rayleigh group velocities in the southeastern margin of the Tibetan Plateau and its tectonic implications. Chin. J. Geophys. 58(5), 1555-1567 (in Chinese).

Farra, V., Vinnik, L., 2000. Upper mantle stratification by P and S receiver functions. Geophys. J. Int. 141, 699-712.

Gan, W., Zhang, P., Shen, Z., Niu, Z., Wang, M., Wan, Y., Zhou, D., Cheng, J., 2007. Presentday crustal motion within the Tibetan Plateau inferred from GPS measurements. J. Geophys. Res. 112, B08416.

Hayes, G.P., Furlong, K.P., 2007. Abrupt changes in crustal structure beneath the Coast Ranges of northern California–developing new techniques in receiver function analysis. Geophys. J. Int. 170, 313-333.

Hazarika, D., Arora, B.R., Bora, C., 2012. Crustal structure and deformation in the northeast India–Asia collision zone: constraints from receiver function analysis. Geophys. J. Int. 188, 737-749.

Hu, S.B., He, L.J., Wang, J.Y., 2000. Heat flow in the continental area of China: a new data set. Earth Planet. Sci. Lett. 179, 407-419.

Hu, J., Su, Y., Zhu, X., Chen, Y., 2005. S wave velocity and Poisson's ratio structure of crust in Yunnan and its implication. Sci. China, Ser. D 48, 210-218.

Hu, J., Yang, H., Xu, X., Wen, L., Li, G., 2012. Lithospheric structure and crust-mantle decoupling in the southeast edge of the Tibetan Plateau. Gondwana Research 22, 1060-1067.

Hu, J., Yang, H., Li, G., Peng., H., 2015. Seismic upper mantle discontinuities beneath Southeast Tibet and geodynamic implications. Gondwana Res. 28(3), 1032-1047.

Kennett, B.L.N., Engdahl, E.R., 1991. Travel times for global earthquake location and phase identification. Geophys. J. Int. 105, 429-465.

Klemperer, S.L., 2006. Crustal flow in Tibet: A review of geophysical evidence for the physical state of Tibetan lithosphere; in Searle, M.P. and Law, R.D. (eds.): Channel Flow, Ductile Extrusion and Exhumation of Lower Mid-Crust in Continental Collision Zones. Geological Society Special Publication 268, 39-70.

Langston, C.A., 1977. Corvallis, Oregon, crustal and upper mantle structure from teleseismic P and S waves. Bull. Seism. Soc. Am. 67, 713-724

Langston, C.A., 1979. Structure under Mount Rainer, Washington, inferred from teleseismic body wave. J. Geophys. Res. 84, 4749-4762.

Lei, J., Zhao, D., Su, Y., 2009. Insight into the origin of the Tengchong intraplate volcano and seismotectonics in southwest China from local and teleseismic data. J. Geophys. Res. 114, B05302.

Lei, J., Li, Y., Xie, F., Teng, J., Zhang, G., Sun, C., Zha, X., 2014. Pn anisotropic tomography and dynamics under eastern Tibetan Plateau. J. Geophys. Res. Solid Earth 119, doi:10.1002/2013JB010847.

Li, X., Yuan, X., Kind, R., 2007. The lithosphere-asthenospher boundary beneath the western United States: Geophys. J. Int. 170, 700–710.

Li, C., van der Hilst, R., Meltzer, A.S., Engdahl, E.R., 2008. Subduction of the Indian lithosphere beneath the Tibetan Plateau and Burma. Earth Planet. Sci. Lett. 274, 157-168.

Ligorria, J.P., Ammon, C.J., 1999. Iterative deconvolution and receiver-function estimation. Bull. Seism. Soc. Am. 89, 1395-1400.

Liu, K.H., Gao,S.S., 2006. Mantle transition zone discontinuities beneath the Baikal rift and adjacent areas, J. Geophys. Res. 111, B11301.

Liu, Q.Y., van der Hilst, R.D., Li, Y., Yao, H.J., Chen, J.H., Guo, B., Qi, S.H., Wang, J., Huang, H., Li, S.C., 2014. Eastward expansion of the Tibetan Plateau by crustal flow and strain partitioning across faults. Nat. Geosci. 7, 361-365.

Meltzer, A. S., Bürgmann, R., van der Hilst, R.D., King, R., Chen, Z., Koons, P.O., Lev, E., Liu,Y.P., Zeitle, P.K., Zhang, X., Zhang, J., Zurek, B., 2007. Geodynamics of the southeastern Tibetan Plateau from seismic anisotropy and geodesy. Geology 35 (6), 563-566.

Molnar, P., Tapponnier, P., 1975. Cenozoic tectonics of Asia: effects of a continental collision. Science 189, 419-426.

Molnar, P., England, P., Martinod, J., 1993. Mantle dynamics, uplift of the Tibetan Plateau and the Indian Monsoon. Rev. Geophys. 31, 357-396.

Rippe, D., Unsworth, M., 2010. Quantifying crustal flow in Tibet with magnetotelluric data. Phys. Earth Planet. Int. 179, 107-121.

Royden, L.H., Burchfiel, B.C., King, R.W., Wang, E.C., Chen, Z.L., Shen, F., Liu, Y.P., 1997. Surface deformation and lower crustal flow in Eastern Tibet. Science 276 (2), 788-790.

Royden, L.H., Burchfiel, B.C., van der Hilst, R.D., 2008. The geological evolution of the Tibetan Plateau. Science 321, 1054-1058.

Schoenbohm, L., Burchfiel, B.C., Chen, L., Yin, J., 2006. Miocene to present activity along the Red River fault, China, in the context of continental extrusion, upper crustal rotation, and lower crustal flow. Geol. Soc. Am. Bull. 118, 672-688.

Sun, C.Q., Lei, J.S., Li, C., Zhang, G.W., Zha, X.H., Li, F., 2013. Crustal anisotropy beneath the Yunnan region and dynamic implication. Chinese J. Geopys. 56(21), 4095-4105 (in Chinese).

Tapponnier, P., Peltzer, G., Le Dain, A.Y., Armijo, R., Cobbold, P., 1982. Propagating extrusion tectonics in Asia: New insights from simple experiments with plasticine. Geology 10, 611-616.

Tapponnier, P., Peltzer, G., Armijo, R., l986. On the mechanics of the collision between India and Asia; in Coward, M.P. and Ries, A.C. (eds.): Collision Tectonics. Geological Society of London Special Publication 9, 115-157.

Tapponnier, P., Zhiqin, X., Roger, F., Meyer, B., Arnaud, N., Wittlinger, G., Jingsui, Y., 2001. Oblique stepwise rise and growth of the Tibet Plateau. Science 294, 1671-1677.

Vinnik, L.P., 1977. Detection of waves converted from P to SV in the mantle. Phys. Earth Planet. Int. 15, 39-45.

Wang, E., Burchfiel, B.C., Royden, L.H., Chen L., Chen J., Li W., Chen Z., 1998. Late Cenozoic Xianshuihe-Xiaojiang, Red River, and Dali Fault Systems of Southwestern Sichuan and Central Yunnan, China. Geol. Soc. of Am., Special Paper 327.

Wang, E.C., Burchfiel, B.C., 2000. Late Cenozoic to Holocene deformation in southwestern Sichuan and adjacent Yunnan, China, and its role in formation of the southeastern part of the Tibetan Plateau. Geol. Soc. Am. Bull. 112 (3), 413-423.

Wang, C.Y., Chan, W.W., Mooney, W.D., 2003. Three-dimensional velocity structure of crust and uppermantle in southwestern China and its tectonic implications. J. Geophys. Res. 108 (B9), 2442.

Wang, C.Y., Han, W.B., Wu, J.P., Lou, H., Chan, W., 2007a. Crustal structure beneath the eastern margin of the Tibetan Plateau and its tectonic implications. J. Geophys. Res. 112, B07307.

Wang, Y., Zhang, X., Jiang, C., Wei, H., Wan, J., 2007b. Tectonic controls on the late Miocene-Holocene volcanic eruptions of the Tengchong volcanic field along the southeastern margin of the Tibetan Plateau. Jour. Asian Earth Sci. 30, 375-389.

Wang, C.Y., Lou, H., Silver, P.G., Zhu, L., Chang, L., 2010. Crustal structure variation along 30°N in the eastern Tibetan Plateau and its tectonic implications. Earth Planet. Sci. Lett. 289, 367-376.

Wessel, P., Smith, W.H.F., 1998. New, improved version of the Generic Mapping Tool released, EOS Trans. AGU 79, 579.

Xu, L., Rondenay, S., van der Hilst, R.D., 2007. Structure of the crust beneath the southeastern Tibetan Plateau from teleseismic receiver functions. Phys. Earth Planet. Inter. 165, 176-193.

Yang, H., Hu, J., Li, G., Zhao, H., Wen, L., 2011. Analysis of the crustal thickness and Poisson's ratio in eastern Tibet from teleseismic receiver functions. Geophys. J. Int. 186, 1380-1388.

Yang, H., Hu, J., Hu, Y., Duan, Y., Li, G., 2013. Crustal structure in the Tengchong volcanic area and position of the magma chambers. Jour. Asian Earth Sci. 73, 48-56.

Yao, H., Beghein, C., van der Hist, R.D., 2008. Surface wave array tomography in SE Tibet from ambient seismic noise and two-station analysis: II. Crustal and upper-mantle structure. Geophys. J. Int. 163, 205-219.

Yao, H., van der Hilst, R.D., Montagner, J.P., 2010. Heterogeneity and anisotropy of the lithosphere of SE Tibet from surface wave array tomography. J. Geophys. Res. 115, B12307.

Yin, A., 2000. Mode of Cenozoic east-west extension in Tibet suggesting a common origin of rifts in Asia during the Indo-Asian collision. J. Geophys. Res. 105, 21745-21759.

Yin, A., Harrison, T.M., 2000. Geologic evolution of the Himalayan-Tibetan orogen. Annual Review of Earth and Planetary Sciences 28, 211-280.

Yuan, X., Ni, J., Kind, R., Mechie, J., Sandvol, E., 1997. Lithospheric and upper mantle structure of southern Tibet from a seismological passive source experiment. J. Geophys. Res. 102, 27,491-27,500.

Yuan, X., Kind, R., Li X., Wang, R., 2006. The s receiver function: synthetics and data example. Geophys. J. Int. 165, 555-564.

Zandt, G., Ammon, C.J., 1995. Continental-crust composition constrained by measurements of crustal Poisson ratio. Nature 374 (9), 152-154.

Zhang, P.Z., 2013. A review on active tectonics and deep crustal processes of the Western Sichuan region, eastern margin of the Tibetan Plateau. Tectonophysics 583, 7-22.

Zhang, P.Z., Shen, Z., Wang, M., Gan, W., 2004. Continuous deformation of the Tibetan Plateau from Global Positioning System data. Geology 32, 809- 812.

Zhang, Z., Bai, Z., Wang, C., Teng, J., Lv, Q., Li, J., Liu,Y., Liu, Z., 2005a. The crustal structure under Sanjiang and its dynamic implications: Revealed by seismic reflection/refraction profile between Zhefang and Binchuan, Yunnan. Science in China (Series D) 48(9), 1329-1336.

Zhang, Z., Bai, Z., Wang, C., Teng, J., Lv, Q., Li, J., Sun, S., Wang, X., 2005b. Crustal structure of Gondwana-and Yangtze-typed blocks: An example by wide-angle seismic profile from Menglian to Malong in western Yunnan. Science in China (Series D) 48(11), 1828-1836.

Zhang, X., Wang, Y., 2009. Crustal and upper mantle velocity structure in Yunnan, Southwest China. Tectonophysics 471, 171-185.

Zhang, Z., Wang, Y., Chen, Y., Houseman, G.A., Tian, X., Wang, E., Teng, J., 2009. Crustal structure across Longmenshan fault belt from passive source seismic profiling. Geophys. Res. Lett. 36, L17310.

Zhang, Z.J., Yuan, X.H., Chen, Y., Tian, X.B., Kind, R., Li, X.Q., Teng, J., 2010. Seismic signature of the collision between the east Tibetan escape flow and the Sichuan Basin. Earth Planet. Sci. Lett. 292, 254-264.

Zhang, Z.J., Deng, Y.F., Teng, J.W., Wang, C.Y., Gao, R., Che. Y., Fan, W.M., 2011. An overview of the crustal structure of the Tibetan Plateau after 35 years of deep seismic soundings. Jour. Asian Earth Sci. 40, 977-989.

Zhang, Z.J., Bai, Z.M., Klemperer, S.L., Tian, X.B., Xu, T., Chen, Y., Teng, J.W., 2013. Crustal structure across the northeastern Tibet from wideangle seismic profiling: constraints on Caledonian Qilian orogeny and its reactivation. Tectonophysics doi:10.1016/j.tecto.2013.02.040.

Zhu, L., Kanamori, H., 2000. Moho depth variations in southern California from teleseismic receiver functions. J. Geophys. Res., Vol. 105, No. B2, 2969-2980.

Figure captions

Figure 1. Topography, major active faults (brown solid lines), earthquakes with Ms ≥ 6.0 since 500 AD to 2014 (circles), and broadband stations (red triangles) in east and southeast Tibet. Key to symbols: F1- Longmenshan fault; F2-Xianshuihe fault; F3- Lijiang-Jinhe fault; F4- Xiaojiang fault; F5- Jinshajiang-Red River fault; F6- Lancangjiang fault; F7-Jiali-Nujiang fault; F8-Sagaing fault; SG-Songpan-Ganzi block; TEC-Tengchong volcano area; EHS-Eastern Himalayan Syntaxis; SY-Sichuan-Yunnan. Red arrows are GPS velocity vectors relative to stable Eurasia (Zhang et al., 2004; Gan et al., 2007) whose respective lengths are not strictly proportional to the velocity value. White arrows indicate possible crustal flow channels (Bai et al., 2010). The inset in the top left corner shows a geographic map of south Asia where the study region is contoured by a rectangle, and where the elevation contours in Tibet and nearby areas are drawn at intervals of 1000 m (red thin continuous lines).

Figure 2. Locations of the earthquakes used in this study on a worldwide map. The events with epicentral distance between 30º and 95º are used for computation of P receiver functions, while those events with epicentral distance between 60º and 150º are used for computation of S receiver functions. The small triangle in the center of the figure marks the location of the study region.

Figure 3. Rotation scheme of the displacement components, converted seismic phases and receiver functions waveforms: (a) Incident rays and different coordinate systems. The north (N) and east (E) components are rotated to the radial (R) and transversal (T) components,

where R is pointing to the event epicenter and T is perpendicular to R (inset in the lower right corner). These two components are then projected onto the orthogonal L and Q components (both in the same vertical plain) with the help of the vertical (Z) component. BAZ is the back azimuth of the event-station pair with respect to the north direction. The angle *i* is the incidence angle of the incoming P-wave. (b) Schematic representation of converted P-to-S phases at the Moho. (c) Theoretical receiver function waveforms (standard notation) recorded at surface.

Figure 4. P receiver functions recorded at stations TEC (a) and MDS (c) (see Fig. 9) after moveout corrected to the reference distance of 67º (ordered randomly). The top panels show the respective stacked traces from phases coming from the Moho (Pms, PpPms, PpPms+PpSms). The black strip along each of these traces gives the ±2σ error (σ is standard deviation). On the right, contour diagrams of *Vp*/*Vs* ratio versus depth (b, d) at intervals of 0.5 constructed by applying the *H*-*k* algorithm. The point marked by a cross indicates the solution both for depth and velocity.

Figure 5. S receiver functions recorded at stations TEC (a) and MDS (b) after moveout correction to a reference distance of 67º (in sequential order), and respective stacked traces (upper panels) in depth domain, where the S_MP and S_LP phases stand out clearly. The black strip along each of these traces gives the ±2σ error (σ is standard deviation).

Figure 6. Contours of crustal thickness (in km) obtained from PRFs (a) and SRFs (b) and standard deviation maps (c, d). The dashed lines represent the regional faults and the small triangles indicate the locations of the broadband stations used in this study.

Figure 7: Contours of the Poisson's ratio obtained from PRFs (a) and standard deviation map (b). The gray shaded area shows Poisson´s ratio values above the global average of 0.24-0.25. The dashed lines represent faults and the triangles indicate station locations.

Figure 8. Stacked PRFs traces at stations located at: (a) northern SYDSB; (b) SG fold system; (c) southern SYDSB; (d) Sichuan Basin; (e) Indochina block (on the west side of Jinshajiang-Red River Fault); (f) eastern Yunnan (on the east side of the Xiaojiang Fault). The thin red strip along each of these traces gives the $\pm 2\sigma$ error (σ is standard deviation). The three-letters codes allow the identification of the stations used in this study (see Fig. 9): stations with IC-LVZ are highlighted in red letters, while stations with weak multiple reverberations are highlighted in blue letters. The dashed lines indicate arrivals of the Ps, PpPs and PsPs+PpSs phases each with its own polarity.

Figure 9. Positions of broadband stations in the study area (circles or triangles, three-letter codes), and mapping of sites where either low velocity (red circles) or weak multiple reverberations in PRFs waveforms (blue circles) are observed. Xu et al. (2007) also detected local IC-LVZ at temporary stations (with MC0 prefix, red squares). The yellow shaded areas (A and B) indicate low-velocity channels detected by joint inversion of Rayleigh waves and receiver functions (Bao et al., 2015). Straight lines P1–P4 represent magnetotelluric profiles performed in the area (Bai et al., 2010), while blue ellipses indicate the positions of high conductivity in the crust along these profiles. The dashed lines represent the regional faults.

Figure 10. Pn-velocity tomography (modified from previous results, Lei et al., 2014). Pms-phase splitting vectors indicate the fast wave polarization direction at 21 temporary

seismic stations in Yunnan (Sun et al., 2013) (lower left quadrant). The scale for splitting time delay is shown in the lower right corner. The dashed lines represent faults.

Figure 11. S-wave velocity models obtained by receiver function inversion at some stations: HUP, Sichuan-Yunnan diamond-shaped block; JMG, Sichuan Basin; YIM, Sichuan-Yunnan diamond-shaped block; YOD, Indochina; LOP, eastern Yunnan (top panels). The dotted lines show the respective initial models for inversion. In the lower panels can be seen the adjustments between radial and synthetic waveforms computed by forward modeling. All fits are above the 90%.

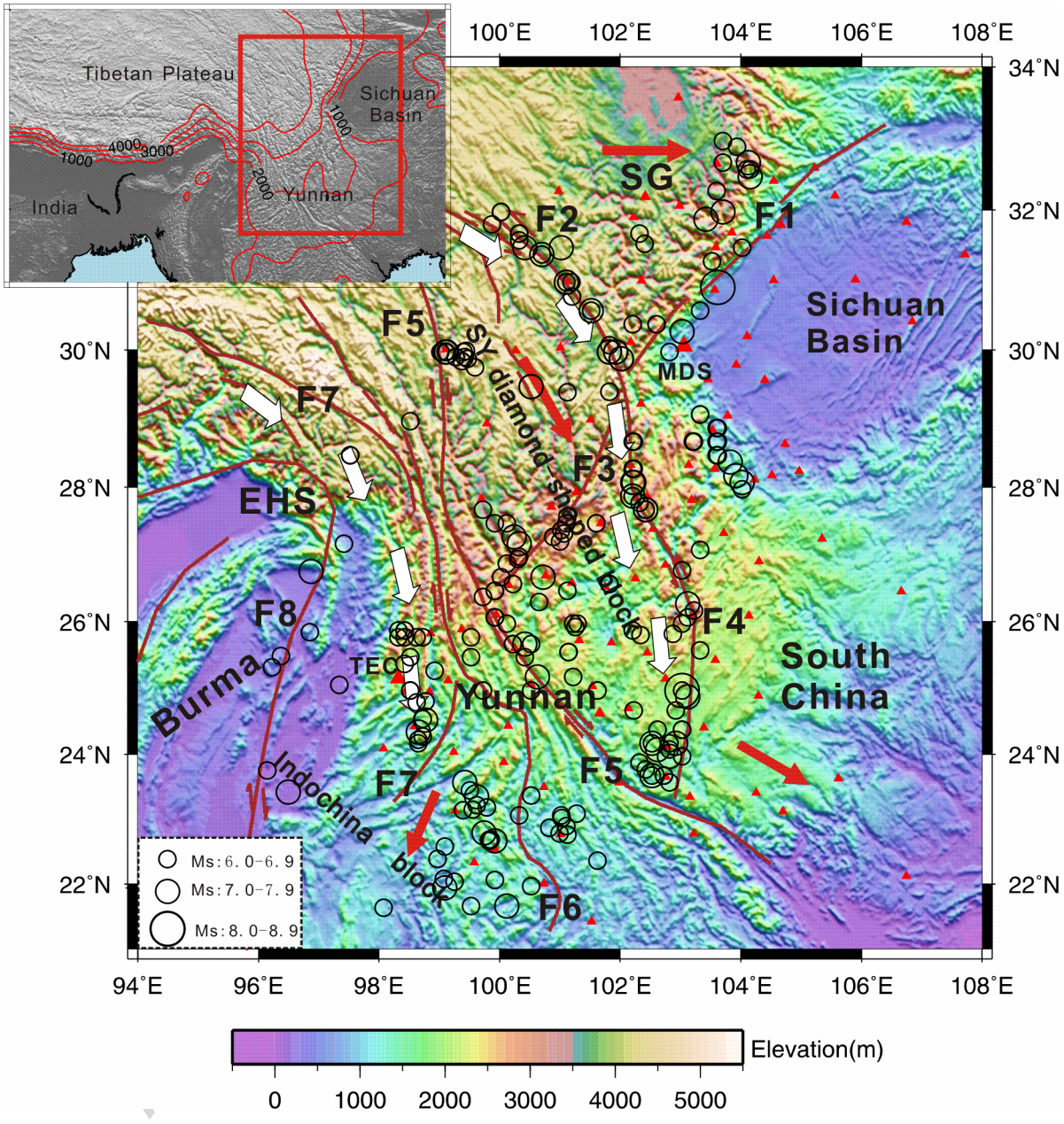
Tibetan Plateau
Sichuan Basin
India
Yunnan
4000
3000
2000
1000
100°E
102°E
104°E
106°E
108°E
34°N
32°N
30°N
28°N
26°N
24°N
22°N
94°E
96°E
98°E
SG
F1
F2
F3
F4
F5
F6
F7
F8
EHS
MDS
TEC
Sichuan Basin
South China
Yunnan
Burma
Indochina block
Sy diamond-shaped block
Ms:6.0-6.9
Ms:7.0-7.9
Ms:8.0-8.9
Elevation(m)
0
1000
2000
3000
4000
5000

Figure 1

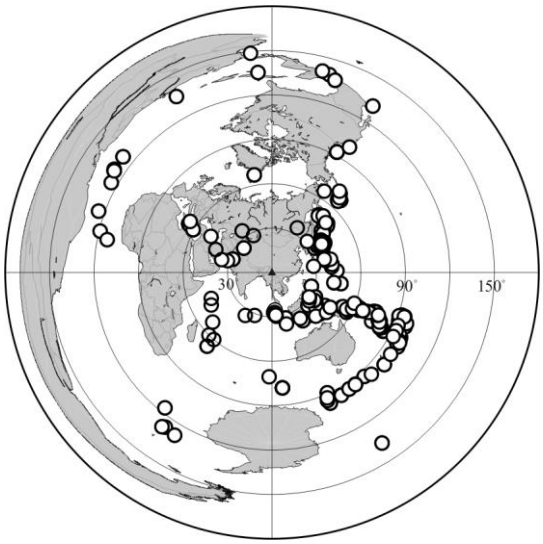

Figure 2

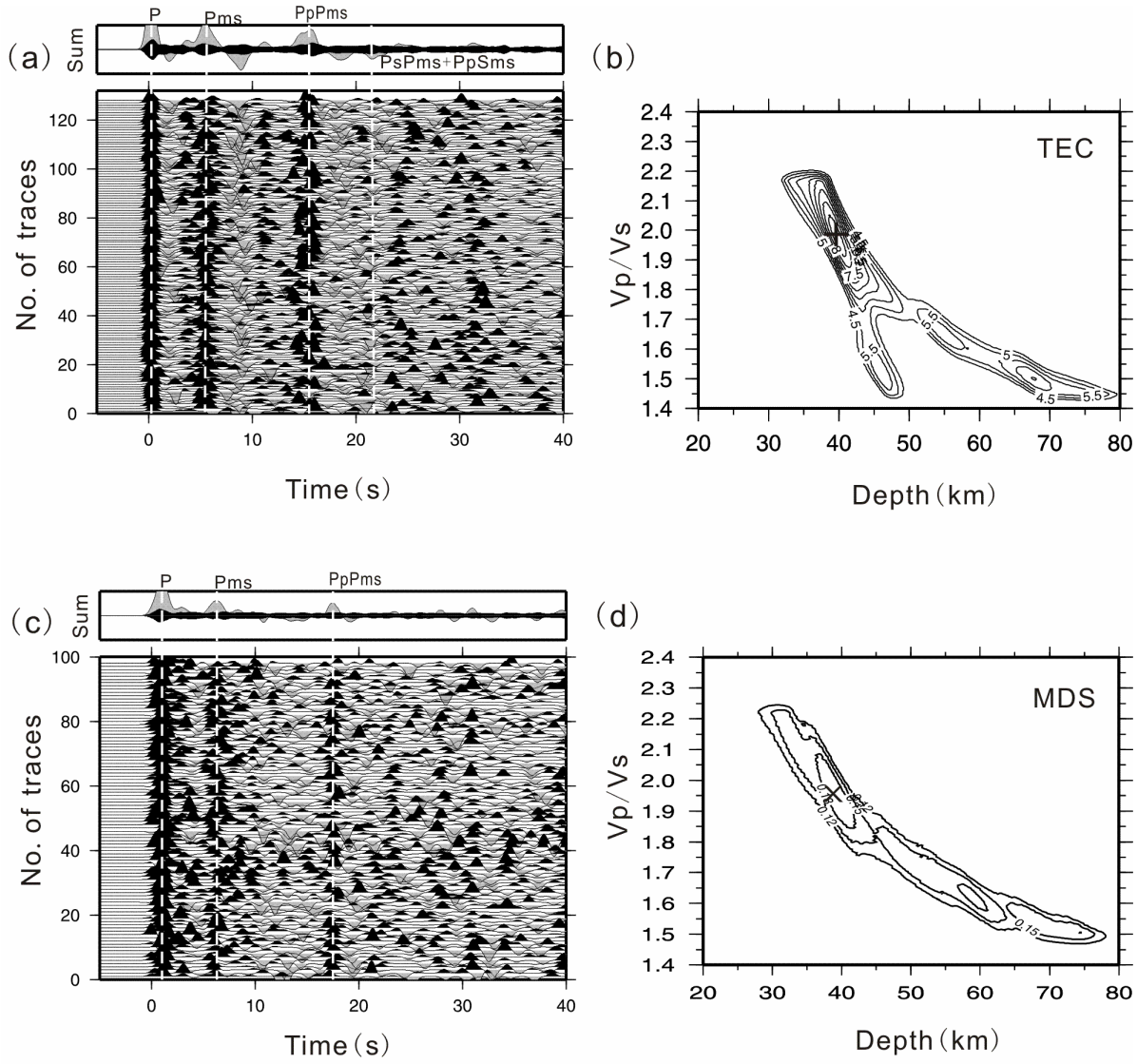

Figure 3

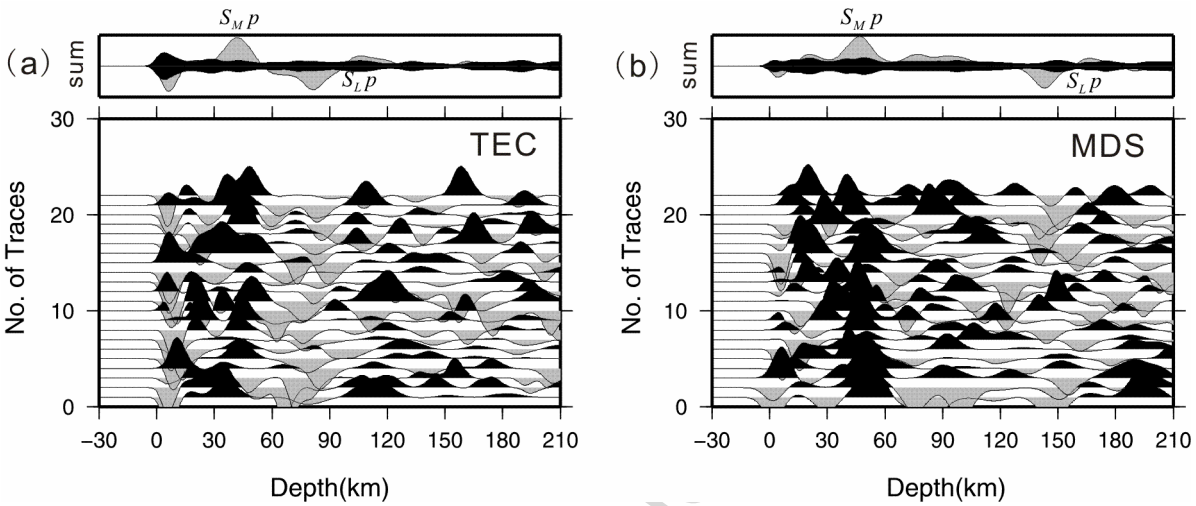

Figure 4

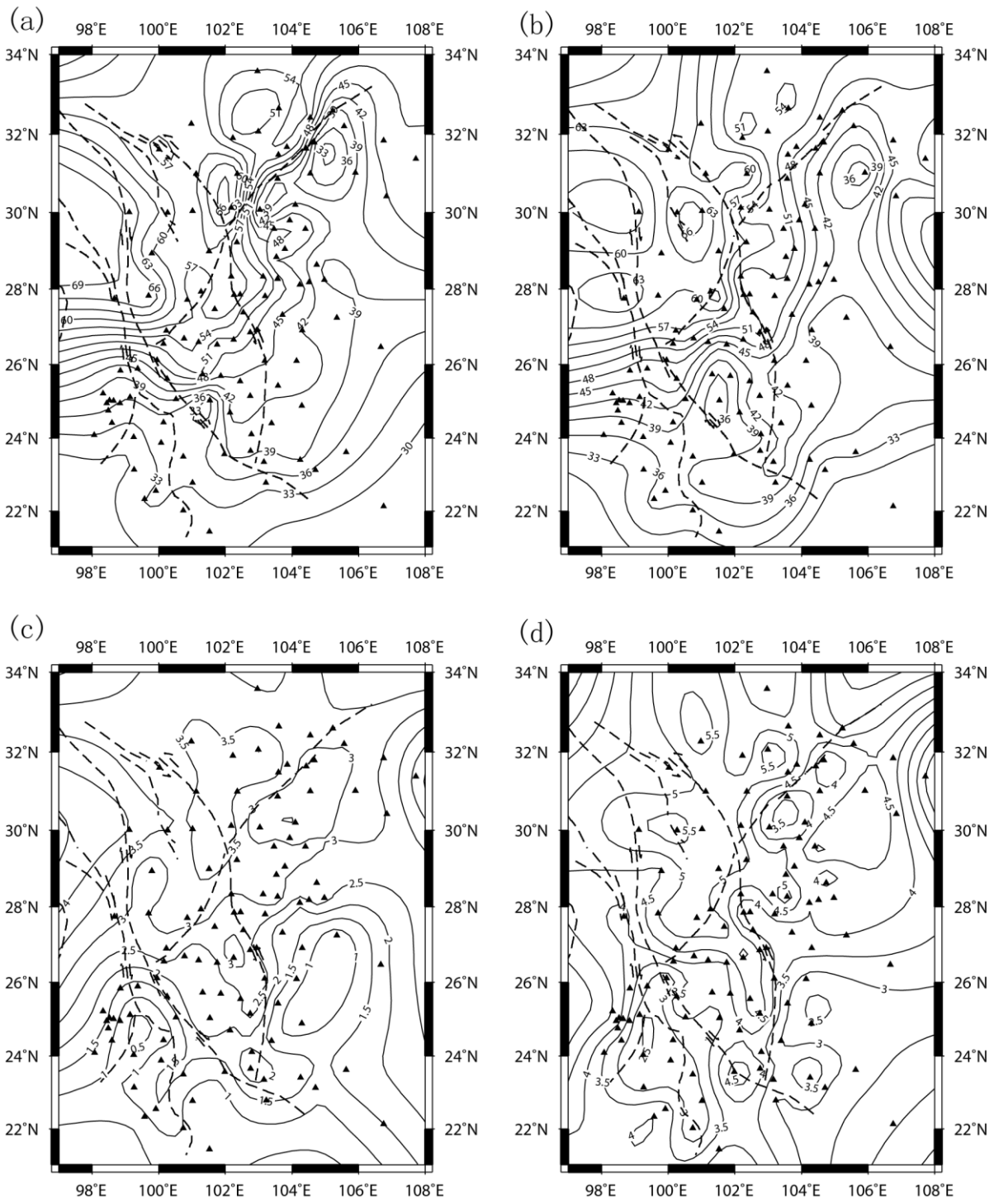

Figure 5

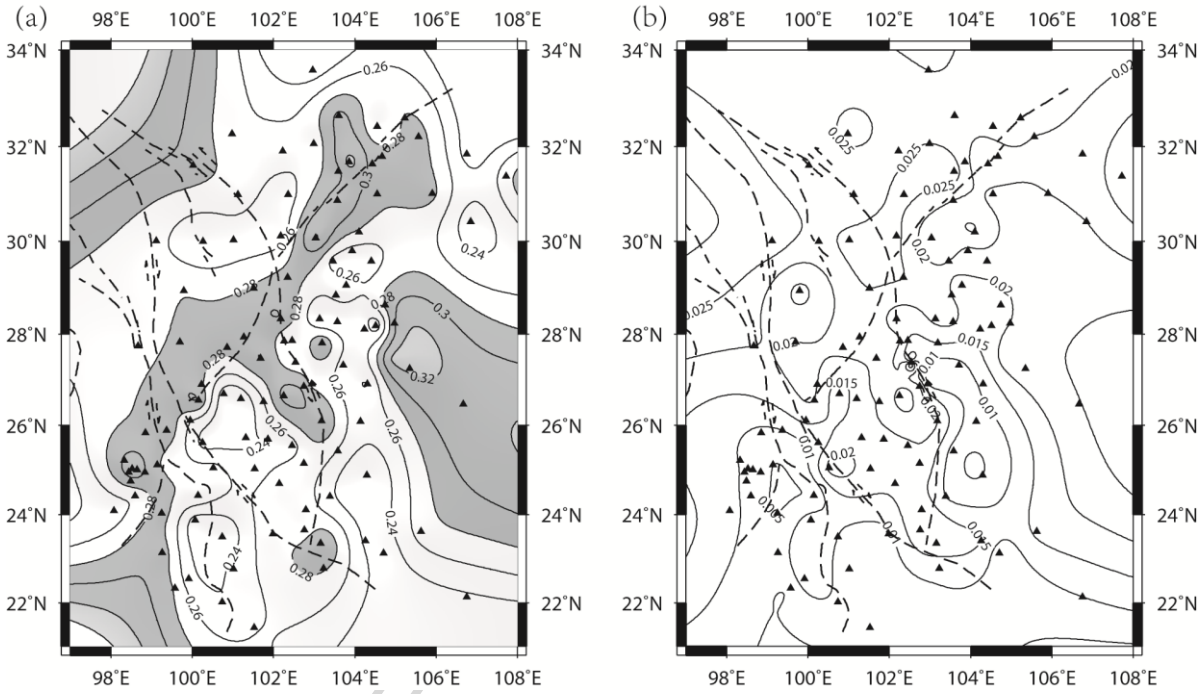

Figure 6

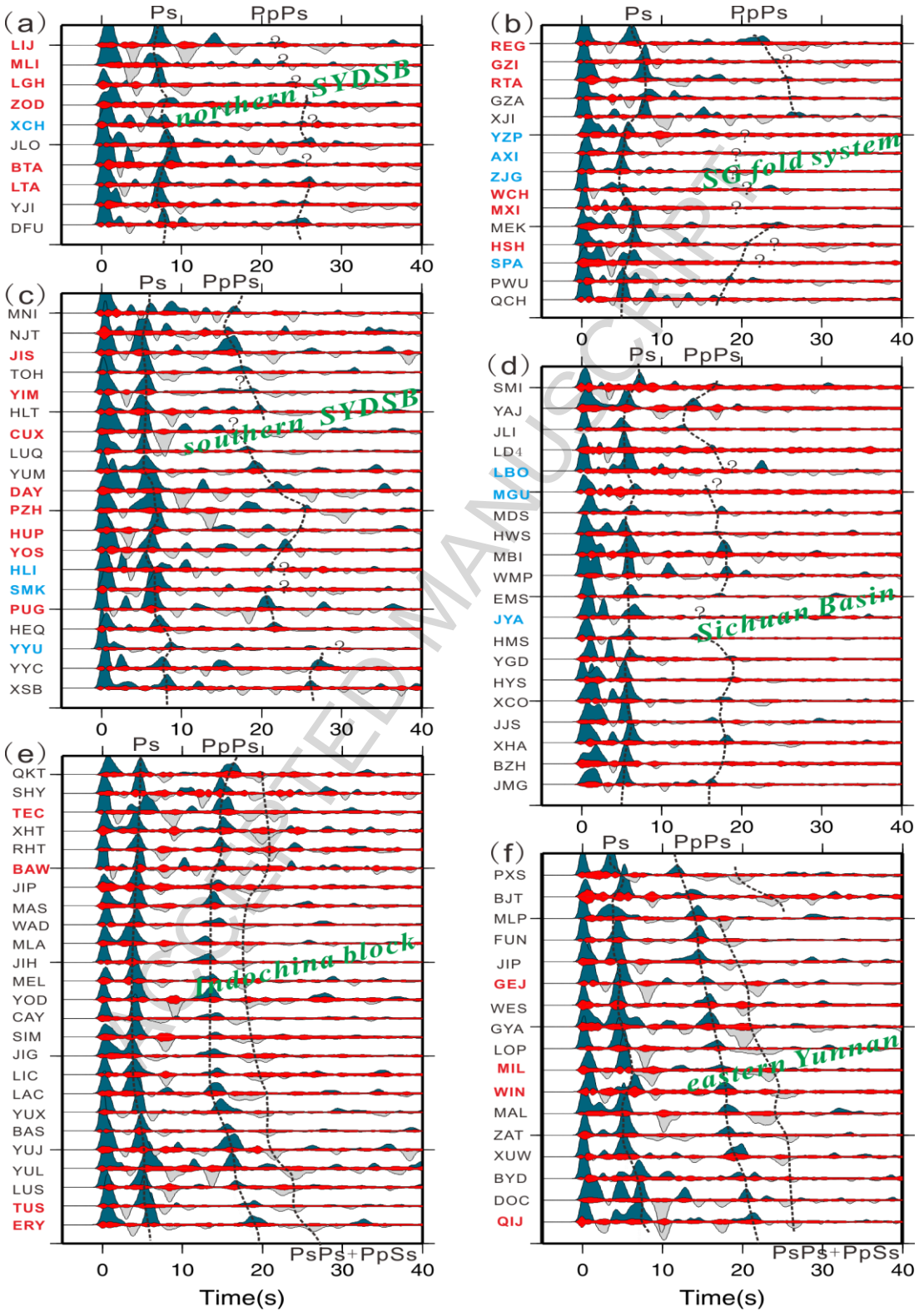

Figure 7

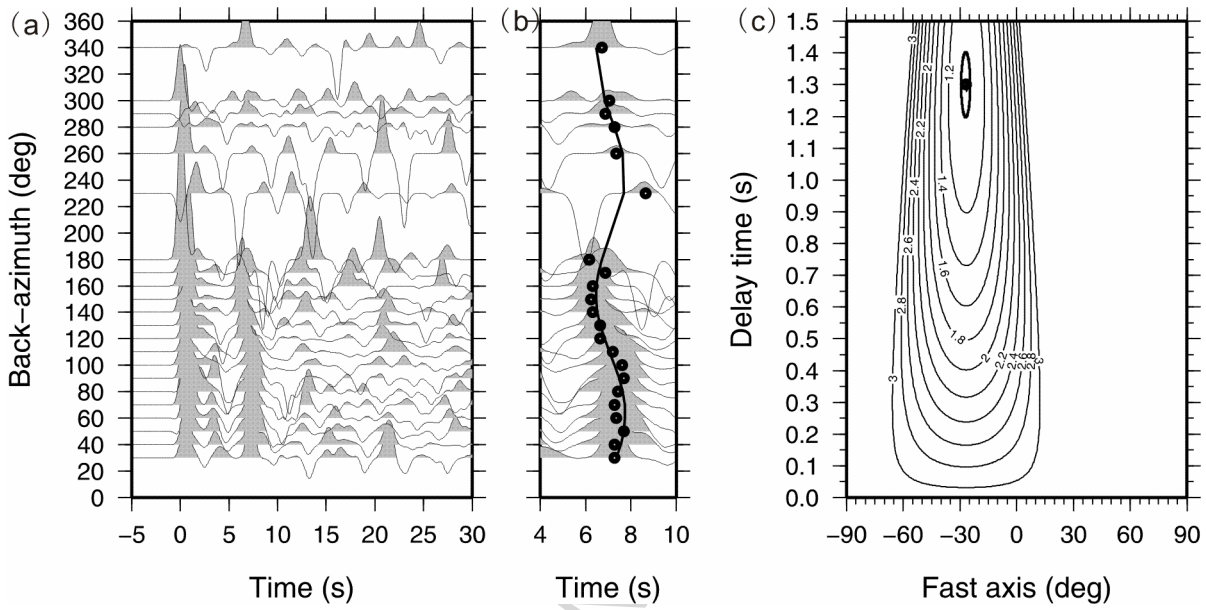

Figure 8

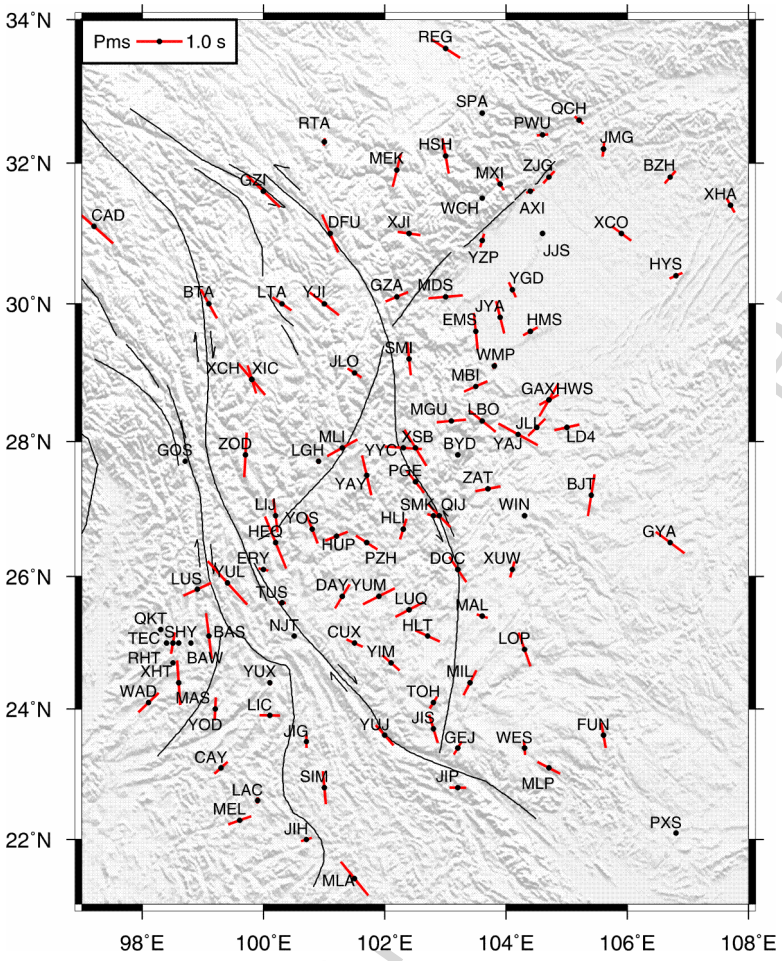

Figure 9

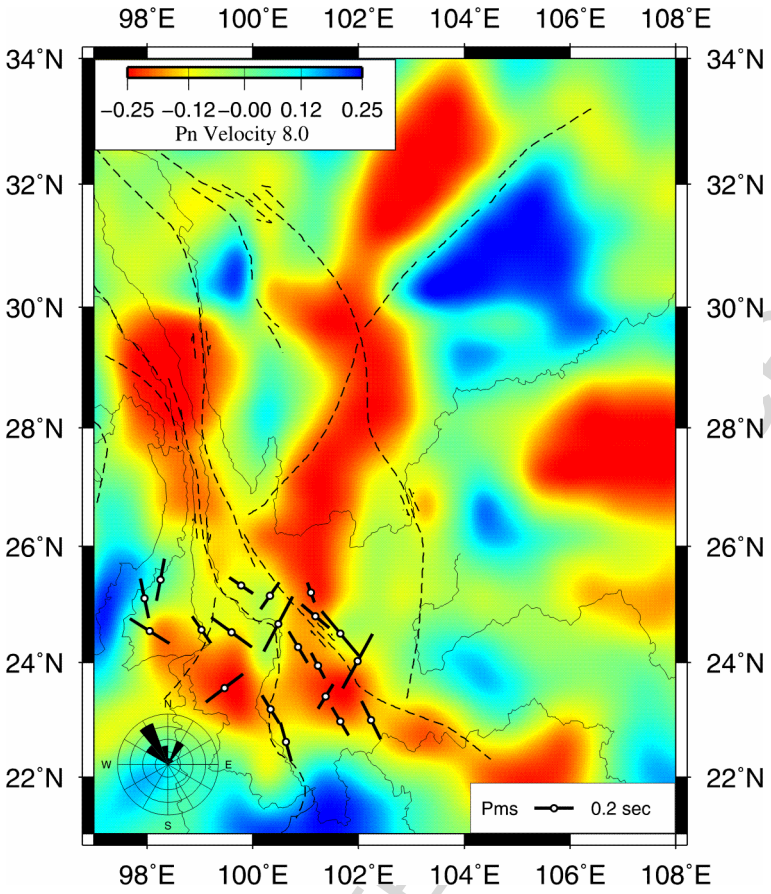

Figure 10

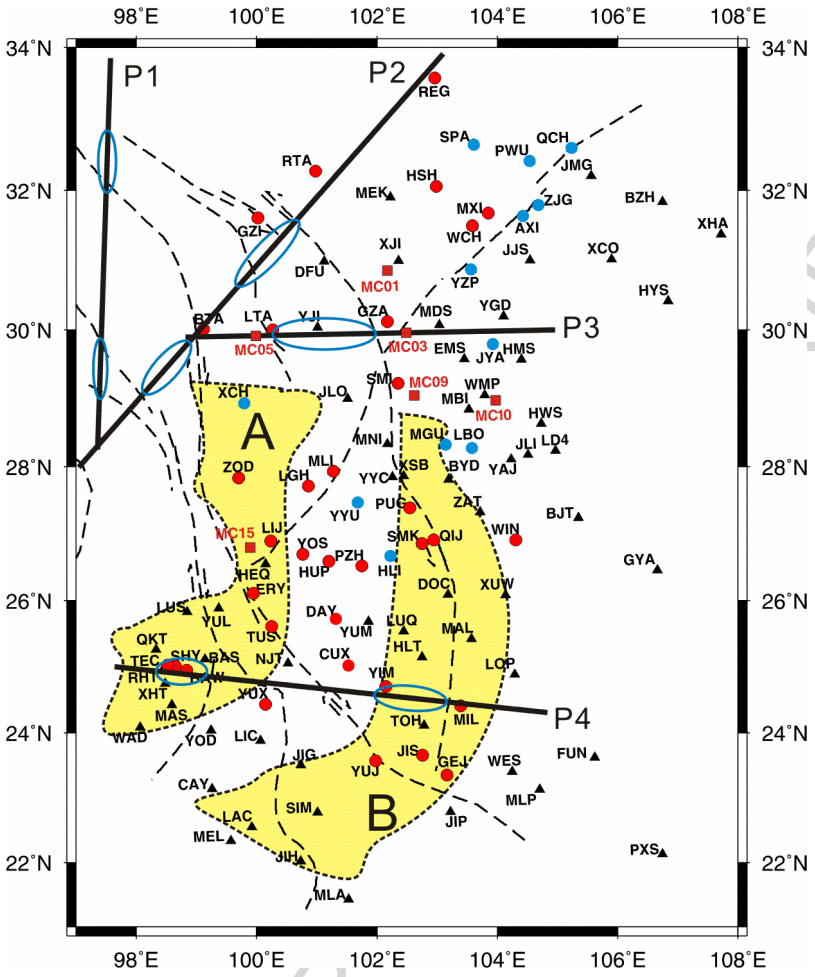

Figure 11

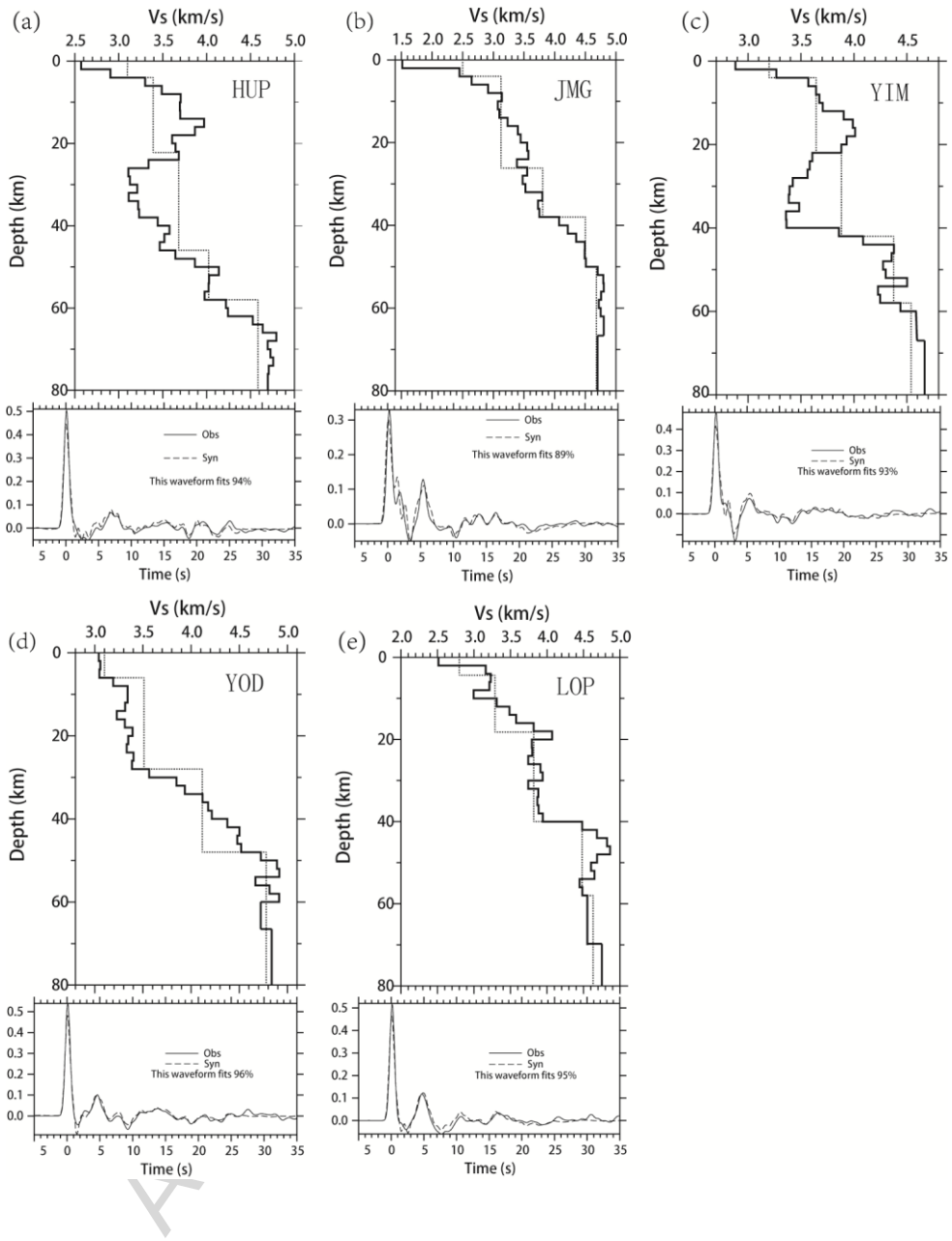

Figure 12

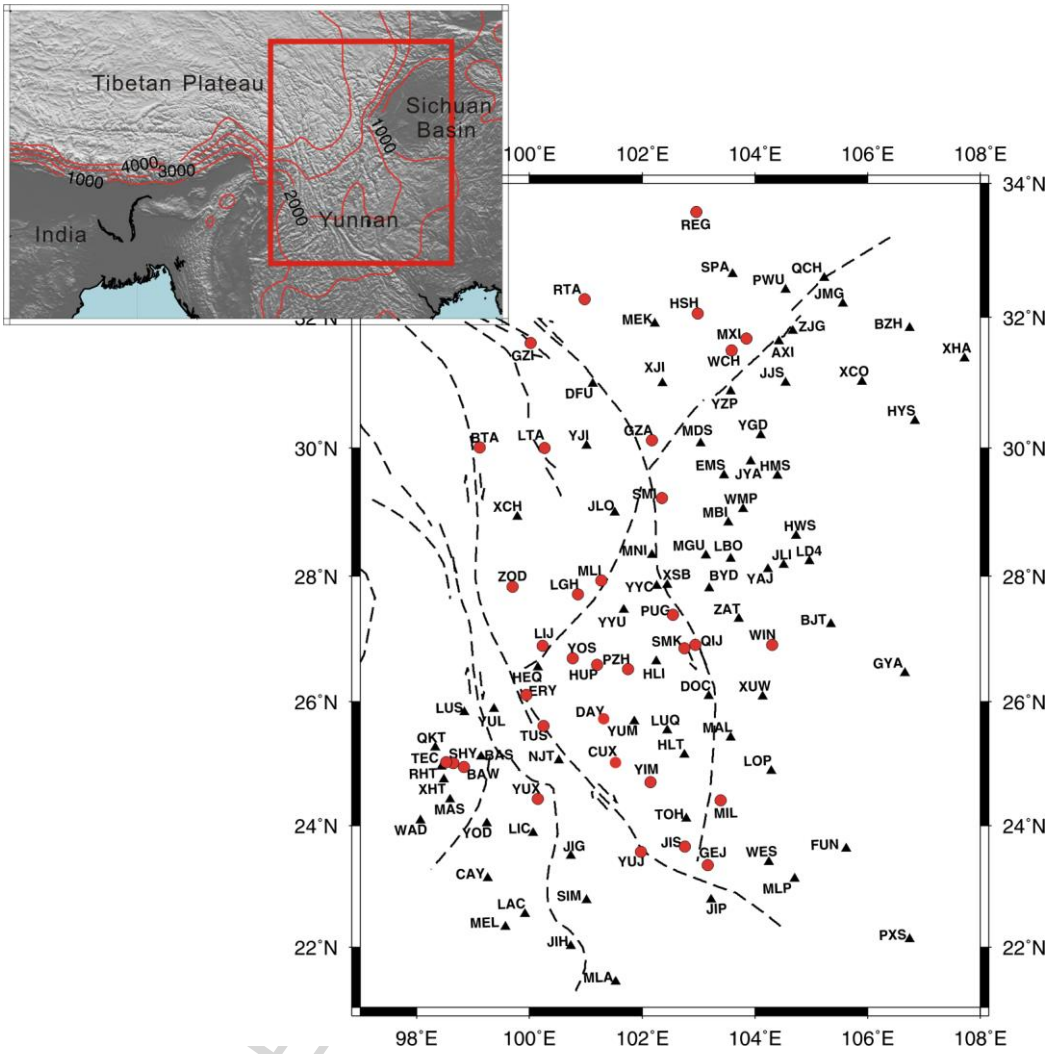

Graphical abstract

Highlights

- Based on P and S receiver functions we have determined the crustal thickness and Poisson's ratio in southeastern Tibet.
- By analyzing the polarity of converted P-to-S phases and crustal reverberation phases we describe the growth and expansion of eastern Tibet.
- Low velocity has been locally detected in a wide region including the east and southeast of Tibet and southern Yunnan.
- We provide seismological evidence of a lower crustal flow advancing southward from the eastern Tibet.
- This flow has invaded widely the Sichuan-Yunnan diamond-shaped block, crossed the Lijiang-Jinhe fault and reached southern Yunnan.